J. Earth Syst. Sci. (2024)133 114
https://doi.org/10.1007/s12040-024-02319-x

Subaerial to subaqueous volcaniclastics from the Bayana sub-basin, North Delhi Fold Belt (NDFB), India: Evidence for a Paleoproterozoic subduction margin

Sagnik Basu Roy[1], Partha Pratim Chakraborty[2,3], Rahul Bailwal[2,*], Ngombi Mavoungou Larissa[4], Kaushik Das[3,4] and Subhajit Sinha[1]

[1] *Department of Geology, Ballygunge Science College, University of Calcutta, Kolkata, West Bengal, India.*
[2] *Department of Geology, University of Delhi, Delhi 110 007, India.*
[3] *Hiroshima Institute of Plate Convergence Area Research, Hiroshima, Japan.*
[4] *Department of Earth and Planetary Systems Science, Graduate School of Advanced Science and Engineering, Hiroshima University, Hiroshima, Japan.*
[*] *Corresponding author. e-mail: rahultherock786@gmail.com*

MS received 10 October 2023; revised 24 December 2023; accepted 29 December 2023

The Paleoproterozoic Jahaj–Govindpura Formation of the Raialo Group of Delhi supergroup, India exposes volcanic and volcaniclastics rock at multiple stratigraphic levels and hence, provides a unique scope for the study of volcaniclastics of varying rheology and their bearing on the tectono-magmatic setting of the basin. From a detailed field study in three spatially disparate sections, associated sedimentary facies types and textural evidences such as clast annealing, deformation in pumice fragments, eutaxitic foliation and shattered crystals, the volcaniclastics are documented as pyroclastic flow (VLC 1), welded tuff (VLC 2), clast-/matrix-supported boulder pyroclastic conglomerate (VLC 3), and pyroclastic fall deposits (VLC 4). Whereas, VLC 1 and VLC 2 are identified as subaqueous, VLC 3 and VLC 4 are grouped under subaerial categories. The facies distribution of volcaniclastics and eastward paleocurrent motif from associated sedimentary facies is indicative of proximal-distal relationship varying between subaerial to sub-marine depositional settings. From collation and comparison of available geochemical data (major, trace element, and REE) of volcanic rock and new geochemical data generated from volcaniclastics under the present study, it is inferred that the source magma was more basic (low SiO_2 and high MgO) resembling tholeiitic to calc-alkaline island-arc source composition while a more intermediate to felsic composition is posited for the volcaniclastics. Considering the ca-1876 Ma time frame of the basin and a subduction-related magmatic character for the volcaniclastics, a possible Orosirian subduction margin, related to the 'Columbia' supercontinent, in the vicinity of the Bayana sub-basin in North Delhi fold belt is suggested.

Keywords. Volcaniclastics rock; Jahaj–Govindpura volcanic rocks; Paleoproterozoic; Raialo group; Columbia supercontinent.

1. Introduction

After the introduction of concepts related to plate tectonics and volcanic arcs, sedimentologists started taking a keen interest in volcaniclastics and their facies variants. Interdisciplinary studies involving fluid dynamics, physical volcanology, hydrology, and geomorphology were initiated to understand the complexity in volcaniclastic origin and emplacement (Fisher 1961, 1966; Cas and Busby-Spera 1991; McCaffrey *et al.* 2001; Branney and Kokelaar 2002; Manville *et al.* 2009; Sulpizio *et al.* 2014; Lenhardt *et al.* 2017, 2020; DeWolfe and Pitmann 2018; Hinchey 2021 and many others). A great impetus in the study of this branch of sedimentology was seen in the 1980s and 90s following some explosive eruptions such as Mt. Pinatubo in the Philippines, Novarupta in Alaska, Mt. St. Helens in the US, and Mt. Taupo in New Zealand. The term 'volcaniclastics' represents all volcanic fragments originated by the processes of volcanic and sedimentary nature. It comprises a range of particles that underwent fragmentation, transport, and depositional processes (Fisher 1984; Cas and Wright 1987; McPhie *et al.* 1993; Manville *et al.* 2009). The sedimentological attributes of volcaniclastic deposits are used for interpretation of (i) the nature of the source volcano (such as phreatic, phreatomagmatic), (ii) transport and depositional mechanisms, (iii) character of the depositional environment, and (iv) post-depositional diagenetic alteration. It is also appreciated that documentation and analysis of volcaniclastic deposits from tectonically active basins, such as rift (where volcanic activity is largely controlled by deep-seated faults and other ancillary structures (Morley 1989; Versfelt and Rosendahl 1989; Lambiase and Bosworth 1995; Gupta *et al.* 1998; Hinchey 2021) and forearc (Garzanti 1986; Sharp and Robertson 2002; Stern *et al.* 2014) among others, may provide important clues on tectono-thermal and paleogeographic history and in turn, may help in basin analysis and modelling. Additionally, the characterization of volcaniclastic deposits from rock records aimed towards understanding the extent and nature of eruption (effusive/explosive), the ambiance of deposition (subaerial/subaqueous), rheology, duration of flow as well as the relief and climate in course of deposition (Pal *et al.* 2005; Manville *et al.* 2009; Houghton and Carey 2015).

Unlike slow fragmentation processes that lead to clastic sediment generation from pre-existing rocks through weathering and erosion, the generation of pyroclastics is instantaneous with subaerial/subaqueous eruption. In the absence of a necessarily slow process of crystallization, metastable glass, and pumice fragments become integral particulate constituents in volcaniclastic deposits. Also, sedimentary responses of particulate matters, generated from the eruptive activity of any volcano in a variety of size grades, depend on the mutual interplay between the character of pyroclastic material (vesiculation, welding, fragmentation) and ambient environmental conditions including physiography and hydrology (subaerial, subaqueous, relief, and climate). After the production of volcaniclastics, depending on their size grade, they either get transported in the form of subaerial/subaqueous density/gravity currents (Druitt 1998; White 2000; McCaffrey *et al.* 2001; Roverato *et al.* 2016, 2017; Lenhardt *et al.* 2017, 2020; DeWolfe and Pittman 2018; Chakraborty *et al.* 2019; Hinchey 2021) or travel in suspension to get settled over a large area in the form of ash fall deposits (De Schutter *et al.* 2015). In most documented volcaniclastic records in literature, nature of fragmentation, transport, and deposition of volcaniclastics are attempted either as subaerial eruption-fed pyroclastic density currents (Sulpizo *et al.* 2014), air-borne suspension settlement on land or sea, (Altermann and Lenhardt 2012) or subaqueous eruption (at cases explosive)-fed density currents (Kokelaar and Busby 1992). However, in the absence of any record of the primary eruptive volcano and diagnostic microstructures, controversy abounds over the terrestrial/subaqueous origin of many volcaniclastic deposits leading to debates in the interpretation of depositional milieu. Additionally, a literature survey reveals that the documentation and characterization of the majority of volcaniclastics are from recent eruptions or quaternary records; descriptions of ancient volcaniclastic deposits, particularly from Precambrian successions, are limited and often notional without much details about the kind of flows and their products (cf. Altermann and Lenhardt 2012; Roverato *et al.* 2017). Depositional/emplacement history, petrography, and geochemistry of volcaniclastics from proterozoic rift basin fills not very well understood despite a few detailed studies that include Baltic Shield margin, Norway; North China Craton; Amazonia Craton, Brazil, and Cuddapah Basin, India (Bergh and Torske 1988; Zhao *et al.* 2002; Roverato *et al.* 2017; Lenhardt *et al.* 2017, 2020; DeWolfe and Pitttman 2018; Goswami *et al.*

2018, 2020; Chakraborty *et al.* 2019; Hinchey 2021). The limited data is attributed to poor preservation, obliteration of diagnostic microscopic features under diagenesis, secondary deformation/metamorphism, and long-term erosion/weathering (Mueller *et al.* 2000).

In this backdrop, present study has been carried out in ∼1 km thick well-preserved volcano-sedimentary package from the Paleoproterozoic (∼1876 Ma; Deb and Thorpe 2004) Jahaj–Govindpura Volcanic rock (JGV) Formation, Raialo Group of the Delhi supergroup, exposed at the Bayana sub-basin of North Delhi Fold Belt (NDFB) over region of 30 km^2. The JGV Formation comprises of basalt, volcaniclastic rocks interbedded with sandstone and siltstone lithounits and the present study is confined to volcaniclastic rocks including lithofacies development pattern, microscopic character and geochemistry. This has enabled us to constrain the tectono-magmatic events during the Orosirian Period (Shields *et al.* 2022) and its relation to the erstwhile position of northwest cratonic India in the late Paleoproterozoic Columbia supercontinent. It is worth mentioning that the ∼1850 Ma giant mafic dyke swarms in North China Craton, Indian Craton, and Canadian shield are considered reliable marker for correlation and reconstruction of Columbia supercontinent (Hou *et al.* 2008). Hence, the objectives of present study include: (i) to distinguish between volcaniclastic characters in different paleo-environmental set-ups (subaerial to sub-aqueous) and (ii) to constrain the tectono-magmatic set-up of the basin.

2. Geological background

Spread over ∼1200 km^2 area in an east–west transect in northeastern Rajasthan, the Delhi supergroup of rocks is exposed in three distinct outcrop belts (sub-basins), namely, Khetri–Ajmer in the west, Alwar–Jaipur in the middle and Bayana–Lalsot in the east (Singh 1988) (figure 1a). Compared to metamorphosed and multi-deformed Khetri and Alwar–Jaipur exposure belts, the Bayana sub-basin is nearly undeformed (only monoclinal rolling of strata in a regional scale on a northwest–southeast trending axial plane; Banerjee and Singh 1977; Singh 1982) and nearly unmetamorphosed (Singh 1988, 1991). At the outcrop and transect-scale, beds are low-dipping; the average amount and direction of bedding dip is 12° towards the north–northeast. Pre-Delhi basement rocks include schist and phyllite, well exposed in the western periphery of the basin. The ∼3 km thick Bayana succession is stratigraphically subdivided into three unconformity-bound groups namely, the Raialo, Alwar, and Ajabgarh, in order of superposition (Banerjee and Singh 1977; Singh 1988, 1991) (figure 1b). The Raialo Group is further subdivided into the lower Nithar Formation (represented by conglomerate and sandstone) and the upper Jahaj–Govindpura volcanic rocks (JGV; represented by sandstone, volcanic rocks, volcaniclastics) Formation (Banerjee and Singh 1977). U–Pb geochronology of zircon grains from a rhyodacite tuff layer present within the Raialo Group allowed Deb and Thorpe (2004) to provide an age of 1876 Ma for crystallization and establish an Orosirian Period for the Bayana succession. A rift basin model with an initial downsag and follow-up active faulting is proposed by Singh (1988) from basin-scale mapping. A continued extension along the center of the Bayana sub-basin led to the cyclic outpouring of volcanic rocks in the form of lava flow (*Aa* and *Pahoehoe* flows) that interrupted the basin sedimentation process (Banerjee and Singh 1977; Singh 1982, 1985, 1988, 1991; Alam and Ahmad 2000). On the basis of petrographic study of sandstone intervals present within the JGV, Alam *et al.* (2006) inferred the mixing of sediments from two sources namely, metamorphosed recycled orogen, i.e., Sambar–Jaipur–Dausa uplift (termed as Dausa uplift; Singh 1982) and syn-depositional basaltic eruptions. Geochemical characterization identified the volcanic rocks in the JGV as basaltic in composition with close affinity to low-Ti continental flood basalts and Proterozoic dyke swarms (Thompson *et al.* 1983; Tarney 1992; Raza *et al.* 2007).

3. Methodology

Overlying shallow-marine sandstones of the Nithar Formation (Singh 1988), the volcaniclastic rocks of JGV are exposed over an area of 25 km^2 encompassing the Nithar, Kair, and Hathori villages around the Bayana town in the form of hillocks, cliffs, and road-cutting sections (figure 1b), and offer an opportunity to undertake documentation of different facies variants and their relationship with associated lithology. Lithofacies types are defined based on lithology (including grain size and texture of volcanic clasts), bed geometry

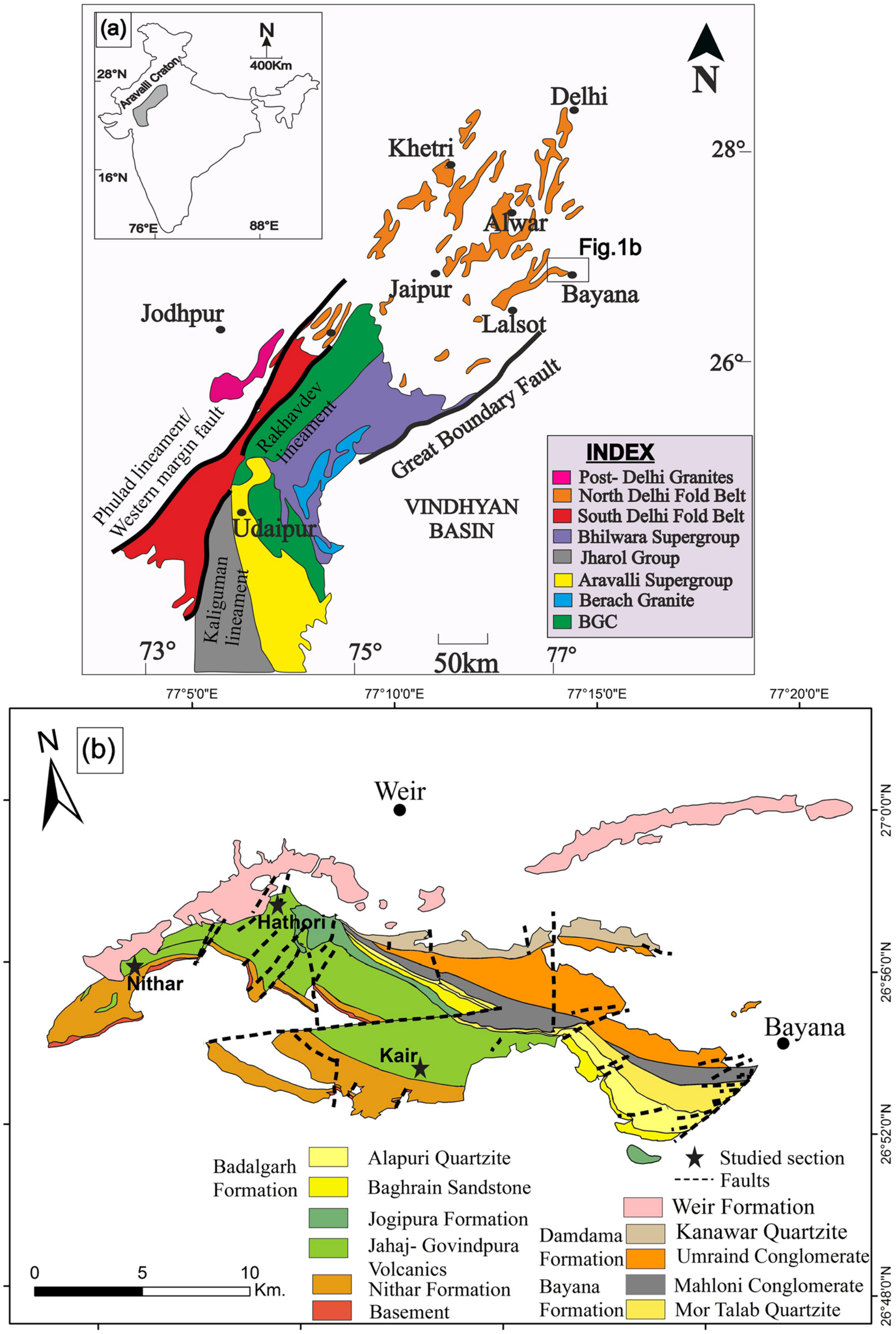

Figure 1. (**a**) Geological map of Delhi Fold Belt (DFB) with geographic location of the Bayana sub-basin marked (enboxed) and (**b**) detailed geological map of the Bayana sub-basin with locations of studied sections marked in asterisks.

(tabular/lenticular), the internal structure (massive/stratified), and grading (normal/reverse). Detailed lithologs including demarcation of volcaniclastics, their associated facies variants, and measurement of paleocurrent vectors, wherever possible, were carried out from all three sections where volcaniclastics are exposed (figures 1b, 2). Photomosaics are prepared to characterize internal structures (both lateral and vertical) within the volcaniclastic beds.

Samples were collected from all facies variants and analyzed for petrography and bulk geochemistry (major and trace elements). Rock samples were polished for petrographic study and crushed into chunks in agate mortar followed by powdering in a TEMA mill. Major element and some trace

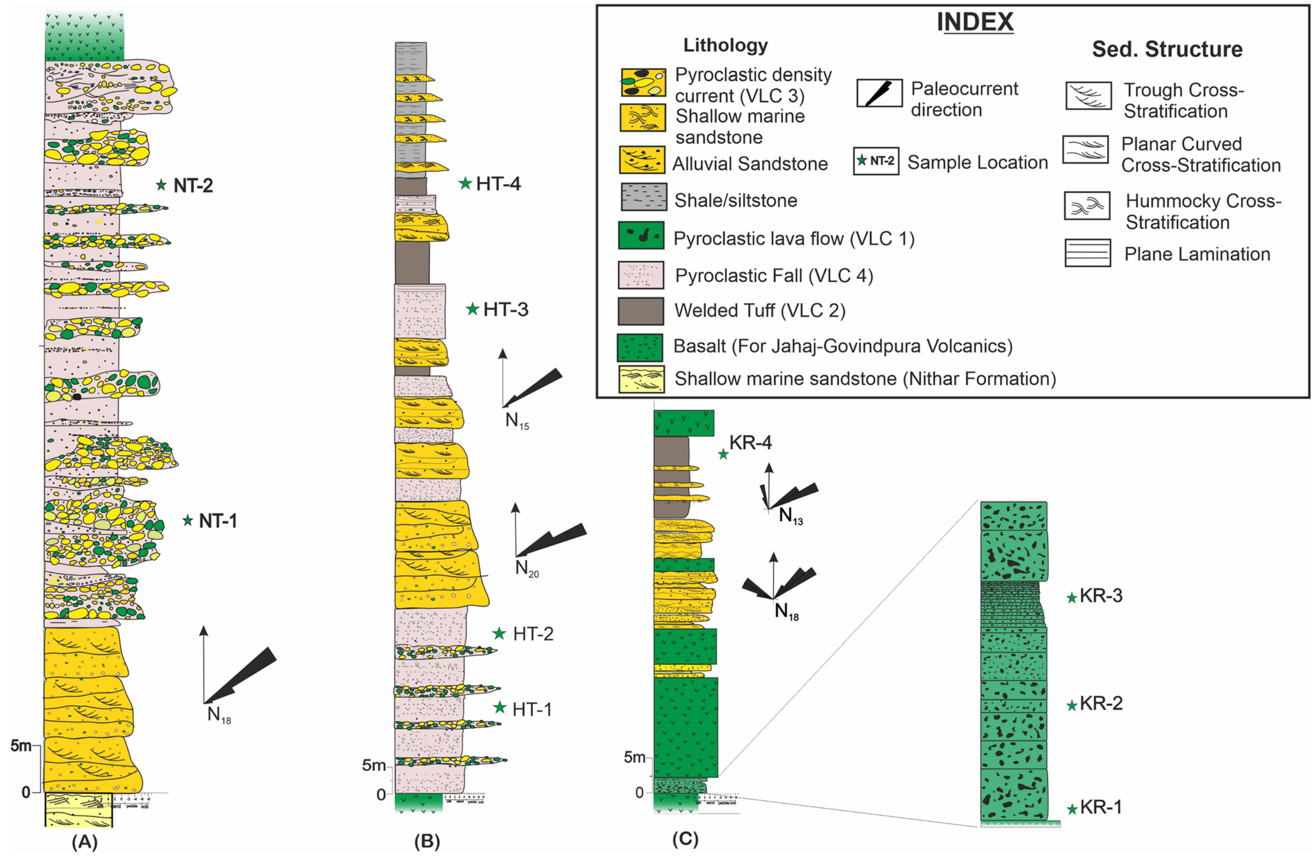

Figure 2. Detailed measured lithologs of studied sections viz. (**A**) Nithar, (**B**) Hathori and (**C**) Kair. Note dominant presence of products of pyroclastic density flows in the westernmost Nithar section and and pyroclastic lava and welded tuffs in the eastern section at Kair. Alluvial deposits in association with volcaniclastics at the Nithar and Hathori sections display consistent north-eastward paleocurrent. Bimodal paleocurrent is recorded in shallow-marine deposits at the Hathori section.

element concentrations were determined by X-ray fluorescence (XRF) using the Rigaku ZSX-101e machine while Rare Earth Elements (REE) were measured by a Thermo Scientific X2 Series® Quadrupole Inductively Coupled Plasma Mass Spectrometer (Q-ICP-MS), installed at the department of Earth and Planetary Systems Science of Hiroshima University, Japan. The XRF analysis was conducted on glass beads that were made using a mix of 2 g of powdered samples with 4 g of lithium tetraborate ($Li_2B_4O_7$) and 0.6 g of lithium nitrate ($LiNO_3$) at the Department of Earth and Planetary Systems Science of Hiroshima University, Japan. More details about the calculation of the Loss of Ignition (LOI), glass beads preparation, measuring instrument characteristics, and analytical precision are given by Mavoungou *et al.* (2022). For ICP-MS analysis, 10–20 mg of the sample powders prepared for XRF analysis were decomposed by different types of acids. The dried samples were dissolved using 5 ml of 5% HNO_3 and 1 ml of the resulting sample solution was taken and diluted into 0.3 ml of indium bismuth (In, Bi) solution and 30 ml of 5% HNO_3. The detailed sample preparation and digestion procedures are described by Chang *et al.* (2003) and Yokoyama *et al.* (1999). The final sample solutions were used for the analysis together with a standard rock sample (JB-2) that served for the determination of the elemental compositions. The accuracy and precision of analyses were >3% for every element, except for yttrium (Y), which was 5% as mentioned by Mavoungou *et al.* (2022). The major and trace elemental compositions are summarized in table 1.

Since the stratigraphic succession studied herein also exposes volcanic rocks, an attempt was made to collate the geochemical characteristics of volcanic rocks and assess genetic kinship between volcanic rocks and volcaniclastics, if any, and to have an idea of the nature of eruption that resulted in both volcanic and volcaniclastic rocks in course of Bayana sedimentation. Geochemical data from the Jahaj–Govindpura volcanic rocks are collated from Raza *et al.* (2007) for comparison and a holistic interpretation.

Table 1. *Major, trace elements and REE composition of the Jahaj–Govindpura volcaniclastics and volcanic rocks.*

Sample ID	NT1	NT2	HT1	HT2	HT3	HT4	KR1	KR2	KR3	KR4	BY1	BY5	BY7	BY9	BY10	BY13	BY15
Elements																	
SiO_2	75.69	85.01	72.99	61.75	54.91	56.73	52.9	51.83	53.35	60.30	50.76	50.13	50.94	50.62	50.6	52.75	51.04
TiO_2	0.81	0.67	0.52	0.74	0.77	1.43	1.27	1.25	1.34	1.26	1.33	1.34	1.46	1.06	1.32	1.83	1.96
Al_2O_3	3.42	4.59	9.20	14.01	17.69	15.67	14.69	14.50	14.18	18.67	11.95	14.84	9.88	11.06	9.96	10.42	10.18
Fe_2O_3	6.06	5.23	5.93	10.64	14.13	16.12	11.39	11.41	11.57	11.22	14.17	11.69	14.16	14.53	14.71	12.66	13.96
MnO	0.01	0.01	0.35	0.20	0.02	0.03	0.14	0.16	0.16	0.09	0.22	0.23	0.21	0.22	0.23	0.2	0.19
MgO	0.13	0.37	1.32	2.31	2.25	1.81	6.56	6.84	7.09	2.36	8.7	7.33	10.26	9.71	10.87	11.02	7.03
CaO	0.03	0.04	1.23	0.54	0.07	0.06	7.02	8.84	7.35	0.14	8.61	7.08	8.04	7.66	10.47	7.76	8.29
Na_2O	0.09	0.03	0.28	0.03	0.08	0.10	3.76	3.92	4.45	0.05	1.64	2.05	1.28	1.64	1.69	2.14	1.49
K_2O	1.33	1.61	5.32	6.58	7.97	6.55	2.45	2.01	1.00	5.13	0.9	0.56	0.52	1.55	0.74	1.86	1.02
P_2O_5	0.04	0.03	0.16	0.38	0.16	0.07	0.15	0.12	0.14	0.10	0.16	0.12	0.13	0.23	0.16	0.18	0.17
Total	87.58	97.58	97.30	97.19	98.03	98.57	100.32	100.88	100.63	99.31	98.44	95.37	96.88	98.28	100.75	100.82	95.33
LOI	1.01	1	2.37	2.41	3.26	2.8	2.85	4.23	2.4	5.27							
Sc	12.44	15.8	21.79	23.5	29.58	32.6	31.83	30.63	34.88	39.47							
V	88.2	69.62	121.47	116.34	169.75	180.53	244.36	246.3	246.06	244.77							
Cr	746.86	536.59	531.8	346.63	190.03	224.55	401.69	356.5	342.35	178.68	374	203	217	397	280	186	110
Co	7.13	4.09	24.39	20.32	13.68	16.44	47.08	45.1	49.96	48.97	30	27	29	32	30	31	27
Ni	16.64	13.93	43.52	59.61	56.62	34.85	81.32	81.02	76.78	74.22	80	75	65	91	45	58	47
Cu	11.88	44.21	9.86	13.77	10.93	4.36	17.95	9.7	34.47	157.36							
Zn	26.78	32.91	91.53	73.43	64.37	55.13	100.72	103.76	101.3	59.04							
Ga	0.85	2.23	7.96	16.92	24.67	25.83	16.97	15.66	16.73	25.37							
Rb	37.39	51.04	102.71	214.74	288.38	294.11	40.87	36.45	21.64	281.8	26	6	17	25	17	59	28
Sr	295.15	17.84	35.24	30.11	36.54	71.62	129.85	126.46	113.65	15.68	221	107	229	22	256	148	1756
Zr	166.24	121.53	106.33	156.46	127	172.53	93.1	91.84	95.17	167.07	55	61	50	88	59	83	139
Nb	7.05	7.35	5.78	14.68	10.42	15.75	5.44	4.57	5.89	12.47	6	9	9	6	9	16	13

Table 1. *(Continued.)*

Sample ID	NT1	NT2	HT1	HT2	HT3	HT4	KR1	KR2	KR3	KR4	BY1	BY5	BY7	BY9	BY10	BY13	BY15
Ba	20882.2	366.06	766.31	1279.98	1806.45	1392.81	418.9	321.87	178.58	356.44	151	83	111	NA	220	527	358
Hf	4.98	1.72	0.62	3.12	0.09	1.97	n.d.	0.45	n.d.	2.27							
Pb	22.77	28.22	7.586	13.3	14.02	23.22	4.046	1.22	6.17	3.18							
Th	7.92	7.28	3.58	12.95	12.56	9.47	1.76	0.63	1.55	10.93	1.45	1.37	1.56	2.01	1.51	2.61	2.61
U	1.58	0.93	0.67	3.05	2.50	2.08	0.36	0.13	0.34	2.94							
Y	3.00	2.87	4.76	15.4	16.96	12.72	17.81	6.39	16.49	17.55	18	17	19	22	19	25	25
Cs	0.63	1.46	0.94	12.69	14.6	10.78	0.84	0.37	0.75	5.73							
La	32.45	32.46	9.855	23.73	44.4	28.88	13.15	4.02	11.79	21.56	11.07	10.02	12.96	12.12	16.87	17.21	16.73
Ce	52.14	58.46	19.52	47.1	85.74	40.71	27.59	8.911	24.87	43.86	22.68	20.76	22.98	23.64	36.08	34.91	32.64
Pr	5.51	6.94	2.37	5.45	10.27	7.11	3.59	1.20	3.20	5.34	2.96	2.81	3.13	3.06	4.72	4.37	3.25
Nd	20.58	29.74	9.50	20.91	39.55	27.4	16.05	5.43	14.32	21.34	13.76	12.47	13.95	14.36	19.91	18.14	13.3
Sm	3.50	6.29	2.05	4.22	7.67	5.53	3.77	1.30	3.48	4.43	3.02	2.73	3.55	3.52	4.96	5.2	3.91
Eu	6.53	1.29	0.74	1.26	1.95	1.73	1.65	0.54	1.28	1.27	1.23	1.08	1.14	1.22	1.45	1.61	1.16
Gd	3.06	3.82	2.05	4.36	7.15	4.94	4.17	1.41	3.80	4.69	3.18	2.79	3.55	3.4	4.38	5.23	3.14
Tb	0.25	0.30	0.24	0.60	0.84	0.64	0.61	0.21	0.57	0.67	0.55	0.54	0.55	0.57	0.78	0.84	0.41
Dy	0.92	0.83	1.14	3.22	3.98	3.23	3.46	1.27	3.28	3.60	2.62	2.9	3.17	3.33	4.59	4.55	2.73
Ho	0.11	0.11	0.20	0.58	0.69	0.57	0.65	0.24	0.61	0.69							
Er	0.33	0.32	0.54	1.70	1.96	1.57	1.80	0.65	1.68	1.98	1.7	1.62	1.91	1.99	2.5	2.35	1.29
Tm	0.04	0.03	0.07	0.22	0.37	0.22	0.24	0.09	0.21	0.27							
Yb	0.32	0.21	0.52	1.51	1.70	1.46	1.35	0.55	1.24	1.86	1.22	1.35	1.29	1.51	1.84	2.05	1
Lu	0.04	0.03	0.07	0.19	0.22	0.19	0.17	0.07	0.15	0.24	0.15	0.18	0.18	0.17	0.28	0.29	0.14
Mg-number	4.14	12.31	30.58	30.01	23.93	18.22	53.25	54.27	54.80	29.41	54.86	55.38	58.92	56.95	59.40	63.28	49.92
A/CAN	0.97	0.99	0.86	0.96	0.99	0.99	0.58	0.53	0.55	0.99							
Molar ratio	2.44	2.68	7.83	8.15	9.12	7.71	14.23	15.77	13.80	6.32	12.15	10.69	10.84	11.85	13.90	12.76	11.80
Zr/Nb	23.58	16.53	18.40	10.66	12.19	10.95	17.11	20.10	16.16	13.40	9.17	6.78	5.56	14.67	6.56	9.19	10.69
Zr/Y	55.38	42.36	22.32	10.16	7.49	13.56	5.23	14.37	5.77	9.52	3.06	3.59	2.63	4.00			
Th/Sc	0.64	0.46	0.16	0.55	0.42	0.29	0.06	0.02	0.04	0.28							
Ti/(Nb*100)	0.69	0.55	0.54	0.30	0.44	0.55	1.39	1.65	1.36	0.61	1.33	0.90	0.98	1.06	0.88	0.69	0.90
$(La/Yb)_N$	72.4	112.05	13.66	11.29	18.71	14.24	6.97	5.26	6.83	8.31	6.51	5.32	7.21	5.76	6.58	6.02	12

Note: Major oxide in wt.%, trace elements and REE in ppm, n.d.= not determined.

Terminology: Volcaniclastic rocks can be classified into flow, surge, and fall types based on particle concentration, sediment transport mechanism and locale of deposition (Burgisser and Bergantz 2002; Nemth and Martin 2007; Sohn and Sohn 2019) or, on the basis of their origin, i.e., (i) primary volcaniclastic rock and (ii) secondary volcaniclastic rocks. Figure 3 demonstrates a genetic classification scheme of volcaniclastic deposits that is followed under the present study (modified from McPhie *et al.* 1993; Gibson *et al.* 1997). Primary volcaniclastic rocks refer to fragmental products formed directly from explosive or effusive eruption through their transport and deposition and secondary volcaniclastics are originally formed by the eruptive volcanic process but before lithification reworked by normal sedimentary processes (mass transport, bedload, or suspension) (Cas and Wright 1987; White and Houghton 2006; Sohn and Sohn 2019). The term 'epiclastic' refers to volcaniclastics derived from the reworking of lithified volcaniclastics or solidified volcanic rocks (Fisher 1966; McPhie *et al.* 1993). For this study, we referred to the term 'volcaniclastics' to include all primary deposits (pyroclastic, autoclastic) that resulted from the eruptive process. Particles that may or may not be volcanic in origin, got eroded along the transport path of volcaniclastics forms secondary volcaniclastic deposits (Fisher 1961; Fisher and Smith 1991). Secondary volcaniclastic deposits are further classified into reworked and reprocessed deposits (after Sohn and Sohn 2019).

4. Volcaniclastic lithofacies

Volcaniclastic rocks can be subaerial or subaqueous or a result of subaqueous deposition from a subaerial eruption (Fisher 1984), however, their distinction between the characteristics products in the rock record always remains subtle and depends either wholly on the depositional set-up of enclosing rock strata (terrestrial/marine) or on the identification of undeniable textures of welding, which commonly signifies subaqueous high-temperature emplacement of volcaniclastics (Kokelaar

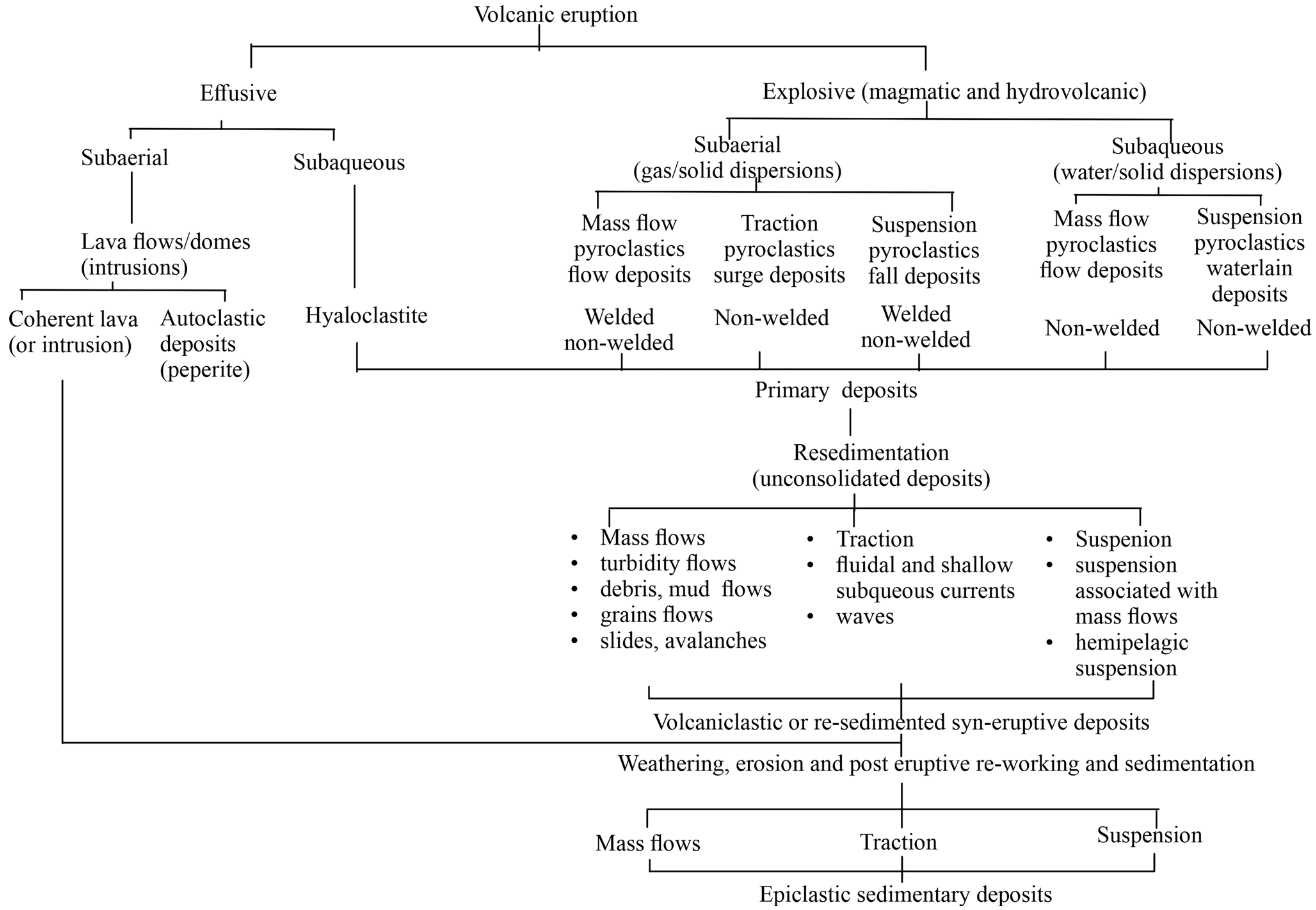

Figure 3. Genetic classification of volcanic deposit erupted in water and air (from Gibson *et al.* 1997).

and Busby 1992). The paleoenvironmental interpretation of Precambrian sedimentary successions in the absence of fossil control often remains subjective, and hence, subaerial/subaqueous interpretation of volcaniclastics present within Precambrian successions becomes tenuous and heavily dependent on the identification of the petrographic features that may suggest welding. Since welding may also result from compaction during diagenesis (Bull and McPhie 2007; Sohn and Sohn 2019), an unequivocal interpretation of the depositional environment for Precambrian volcaniclastics often remains elusive. Keeping this in mind, an attempt has been made to define and classify the volcaniclastic units in terms of their depositional setting, flow rheology, and other operative processes in the course of depositional history. Table 2 illustrates the volcaniclastic and sedimentary lithofacies types delineated under the present study.

Negligible metamorphism and deformation in Bayana strata allowed excellent preservation and delineation of volcaniclastic deposits with varying characters from the JGV Formation. In the study area, a wide spectrum of primary and secondary volcaniclastics representing the pyroclastic flow, fall, surge, and density currents are recorded in association with volcanic rock and sandstone units. On the basis of sorting, composition, clast morphology, transport mechanism and associated sedimentary packages the volcaniclastic packages of JGV are grouped under two broad environmental settings: subaqueous and subaerial.

4.1 *Primary volcaniclastic deposits*

4.1.1 *Subaqueous deposits*

4.1.1.1 *VLC I: Pyroclastic flow deposit*

Description: The best exposure (max. thickness ∼2 m) of this facies is recorded at the outskirt of the Kair village (figures 1b, 2). Green-grey to dark green coloured, amalgamated, thick-bedded, massive units, decimeter-scale in thickness (figure 5a), in alternation with basaltic flows and fine to medium-grained, well-sorted sandstone represent this lithofacies. The interbedded sandstones are lenticular in bed geometry with bedding planes mantled by symmetric wave ripples (average wavelength 3 cm and amplitude 0.5 cm). Internally, trough cross stratifications within the sandstone assume chevron geometry; cross-stratifications record bidirectionality pointing towards NW and NE (figure 4a; lithofacies SS 2; table 2). Internally the pyroclastic deposit is composed of plagioclase laths, pyroxene, devitrified rough-textured sub-angular to sub-rounded magma blobs, glass fragments (pumice; 0.5–4.0 cm in length), often chloritized, and spherical to slightly ovoid-shaped vesicles filled with secondary minerals like calcite, quartz, and zeolite (figure 5b–d). Volcanic clasts (glass fragments) are mostly elongated, irregular, and heavily chloritized. Juvenile vesiculate pumice, lithic crystals, and green to black lapilli are noticed abundantly in the groundmass (figures 5a and 6c). Clastics (2–45 mm in size), disordered in distribution and with edge angles, account for 10% to 48% in volumetric proportion and are cemented by lava (figure 5e and f). Fiamme texture is well observed in the form of flattening of glassy non-vesiculated juvenile clasts. Also, particle agglutination and coalescence along the boundary of droplet-shaped pumice fragments are well noticeable (figure 5g). In cases, plagioclase laths were found enclosing the groundmass containing glass and microlites assuming sub-porphyritic texture (figure 5h). Often glassy parts are devitrified into secondary phases including chlorite, palagonite, or cryptocrystalline quartz and plagioclase feldspar.

Both lithic crystals and pumice fragments display a cyclic distribution pattern in terms of an upward decrease in size and frequency (varying from ∼40 cm near the base to a cm at the top of each cycle) that defines fining-upward normal, coarse-tail grading. Within the available outcrop limitation, three such fining-upward cycles are delineated with each cycle about a meter thick. Whereas agglutinated pumice fragments (*armored lapillae*) are found concentrated at the basal part of cycles, pumice fragments in the upper part of each cycle are non-particulate and smaller in size.

Interpretation: The crystal, crystal fragment (∼35% in abundance) and volcanic glass rich volcaniclastic deposit with vugs, in abundance, is identified as a product of high-temperature pyroclastic flow, derived either directly from the magma or from wall of near surface conduit (Branney and Kokelaar 1992). The elongated and irregularly floating volcanic clasts are indicative of slow solidification during the flow and elongation along the flowing direction (Hao *et al.* 2022). The inward growth of crystals within the vugs suggests vapour-phase crystallization with a large crystal of calcite at the periphery and a gradual decrease in grain size towards the center (figure 5d). Normal (coarse-tail)

Table 2. *Description and interpretation of lithofacies in Jahaj–Govindpura Formation, Raialo Group.*

Unit no.	Lithofacies name	Salient characters	Interpretation
Volcaniclastic lithofacies			
Primary volcaniclastic facies (subaqueous deposits)			
VLC 1	Pyroclastic flow deposit	Meter thick, green grey to dark green coloured. In alternation with basaltic flow and wave rippled sandstone. Internally composed of plagioclase laths, pyroxene, devitrified angular to sub-angular magma clasts, glass fragments (pumice; 0.5–4.0 cm in length), often chloritized. Spherical to ovoid-shaped vesicles filled with secondary minerals. Lithic and pumice fragments display normal grading.	High-temperature pyroclastic flow; volcanic clasts and pumice-rich volcaniclastic deposits, identified as juvenile pyroclasts. Inward crystal growth within vugs indicates vapour-phase crystallization. Petrographic signature of agglutination points towards fluidal and sufficiently hot characters of lithics that led to welding irrespective of post-emplacement cooling and loading.
VLC 2	Fine-grained welded tuff	Extremely fine-grained (below 20 μm in size), buff or dark greenish grey colour rock in alternation with basalt and wave-rippled, cross-stratified sandstone. Internally composed of elongated grey to black coloured fiamme (flattened pumice lenticles), crystals (quartz and plagioclase), pyroclasts (100–150 μm in size) and angular vitroclasts (50–100 μm). Flattened pyroclastic fragments and shards are bow-tie shaped with thread-like terminations, often altered/devitrified to sericite, chlorite, and opaque oxide.	Flattening and attenuation of shards and pumice fragments around quartz, and feldspar clasts suggests viscous attenuated flowage under syn-depositional welding. A subaqueous origin for the welded tuff unit is argued from (i) the wave-dominated shallow-marine origin of associated sedimentary strata, (ii) occurrence of rip-up angular shale clasts, and (iii) presence of pumice clasts with elongated streaked/ fibrous textured fiamme.
Secondary volcaniclastic facies (subaerial deposits)			
VLC 3	Pyroclastic debris current (PDC) deposit/pyroclastic volcanic breccia (Lahar)/pyroclastic debris/mass flows	Heterogeneous bouldery and pebbly (block and bomb; >64 mm) conglomerates with varying degrees of clast concentration. As massive or graded (normal and inverse) unit present in alternation with facies VLC 4 or facies VLC 2. Poorly sorted, subrounded to rounded block- and bomb-sized fragments of pyroclast, basalt, sandstone, and vein quartz, in decreasing order abundance with matrix being an aggregate of sandy to granular lithic (pyroclastic lapilli, basalt, sandstone), crystal (feldspar, quartz) and glassy (pumice) fragments. Most of the pumice clasts are sub-angular to angular. Distribution of smaller clasts in the matrix is controlled by the shape and orientation of larger clasts, upper and basal contacts of conglomerate units are either sharp, planar, and non-erosional or rugged with boulders of the conglomerate units protruding within the underlying VLC 4 layers. Good positive correction ($r^2 = 0.87$) between clast size and bed thickness of conglomerate units.	Products of pyroclastic debris currents (PDC) in which clast entrainment and segregation are dominated either by matrix strength or by granular flow. A plastic to turbulent flow character is surmised from the non-erosional/erosional basal character of conglomerate beds. Isolated clasts at a high angle to the bedding are elutriated under high fluid (gas) pressure. From a positive correlation between clast size and bed thickness an increase in eruptive discharge with the increase in flow competence is inferred.

Table 2. *(Continued.)*

Unit no.	Lithofacies name	Salient characters	Interpretation
VLC 4	Pyroclastic fall deposits	Thin ($\leq$6 cm in thickness) beds of granular (with strewn pebbles) reddish colored deposit (VLC 4a) in alternation with fine-grained yellowish ash deposit (VLC 4b). Plane parallel beds of the facies mantle the underlying relief. Lithic fragments, crystals, glass shards, pumice, and iron oxides in variable proportion and with poor grain sorting constitute the facies. Accretionary (armoured) lapilli with aggregates agglomerated around coarse ash particles is a common observation.	Pyroclastic fall deposition from a spasmodic, non-sustained eruption with many short-lived pulses. Coarse grain size, poor grading, lack of internal structure, and lack of basal scour in VLC 4a suggest the operation of high-concentration pyroclastic fall. Rapid settlement may result in coarse-grained, massive, normal-graded character without any internal structure. The rusty/reddish color with alteration of iron oxide minerals supports the coloration of the facies under a high-temperature thermal effect.
Sedimentary lithofacies			
SS 1	Trough cross-stratified poorly sorted sheet sandstone	In association with volcaniclastic lithofacies VLC 3; medium- to coarse-grained arkosic sheet sandstones with poor grain sorting, internally planar and trough cross-stratified. Paleocurrent measurement from trough cross-stratifications point towards northeast.	Sheet geometry, poor grain size sorting and trough cross-stratification point towards a continental fluvial origin.
SS 2	Chevron cross-stratified moderate to well sorted lenticular sandstone	Moderate to well-sorted sandstones with lenticular bed geometry and symmetric ripples on bedding plane surfaces. Internally chevron cross-stratified with bimodal paleocurrent directing NW and NE. In association with VLC 1 and VLC 2.	Product of wave dominated shallow marine setting; Chevron cross-stratification with bimodal cross-stratification and symmetric wave ripples bear indication of wave domination.

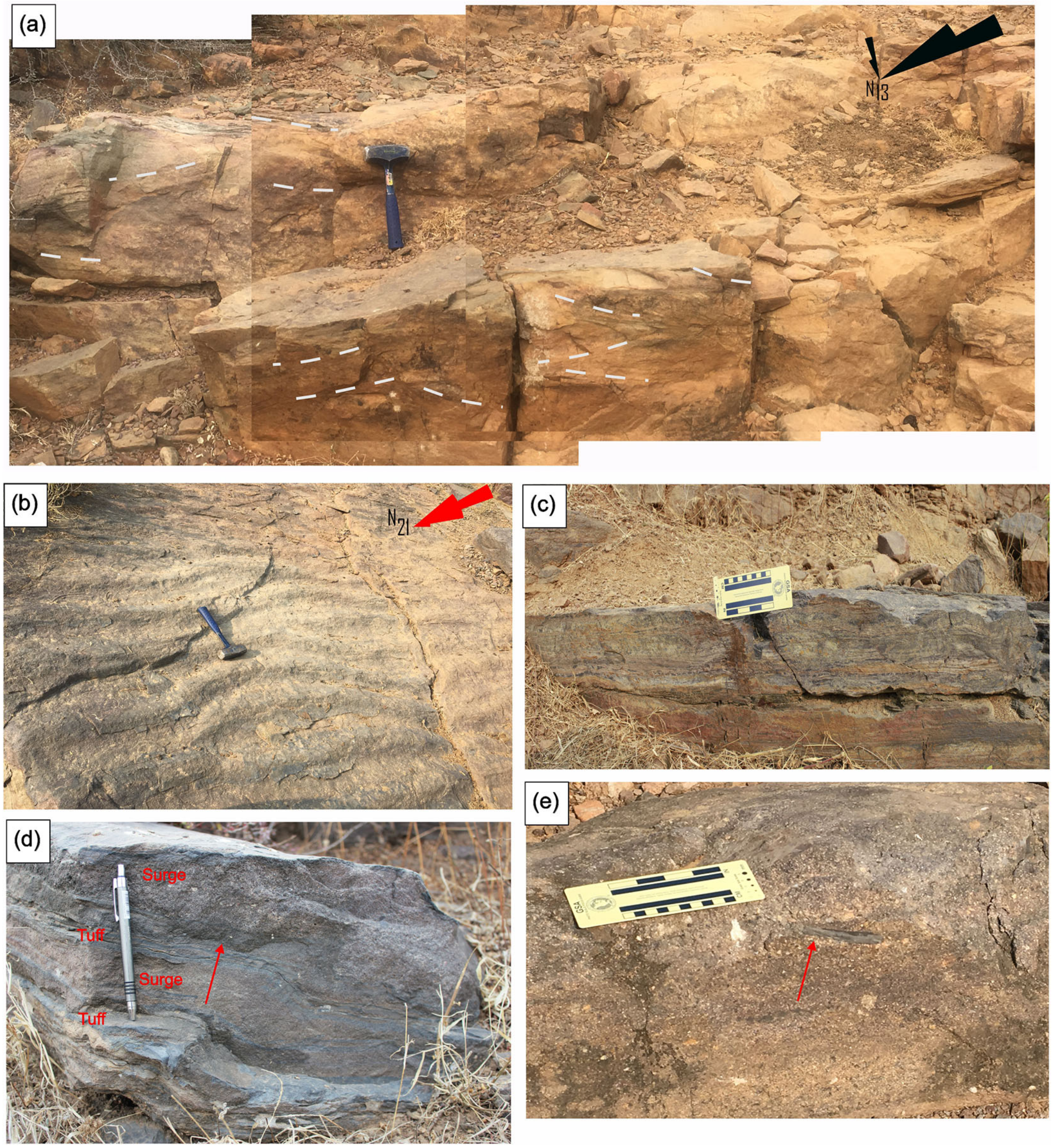

Figure 4. Field photographs illustrating (**a**) chevron cross-stratification with bimodal paleocurrent in shallow marine sandstone in association with volcaniclastics at the Hathori section, (**b**) combined flow ripple on the bedding plane of shallow marine sandstone, (**c**) alternation between fine-grained tuff and granular surge deposit from the Hathori section. Note erosional base of surge deposit (arrowed) at cases, (**d**) horizontally laminated welded tuff at the Hathori section, and (**e**) a close view of granular pyroclastic surge deposit, note presence of tabular outsized lithic fragment (arrowed) floating in groundmass.

grading defined by lithic and pumice fragments may be the result of changing lithic and pumice supply to the depositional boundary layer of the flow in a waning condition either because of diminished explosivity *vis-a-vis* wall rock erosion in the conduit or due to burial and peneplanation of hinterland landscape by aggrading tuff (Branney and Kokelaar 1992). A clear petrographic signature indicating agglutination points towards fluidal and sufficiently hot character of lithics that led to welding irrespective of post-emplacement cooling and loading (Mahood 1984; White and Houghton 2006). The presence of vugs in large frequency, filled with secondary minerals, suggests a gradual change in the viscosity and strength of hot glass as temperature decreases and volatiles exsolve. Progressive aggradation of fining-upward units bears an indication of unsteady flow character with fluctuating input that resulted in stepwise deposition comprising multiple layers (similar to layer 2 of Sparks 1976).

4.1.1.2 *Welded tuff (Pyroclastic fall deposits)*

Description: In alternation with basalt and wave-rippled (ripple index < 10:1), cross-stratified

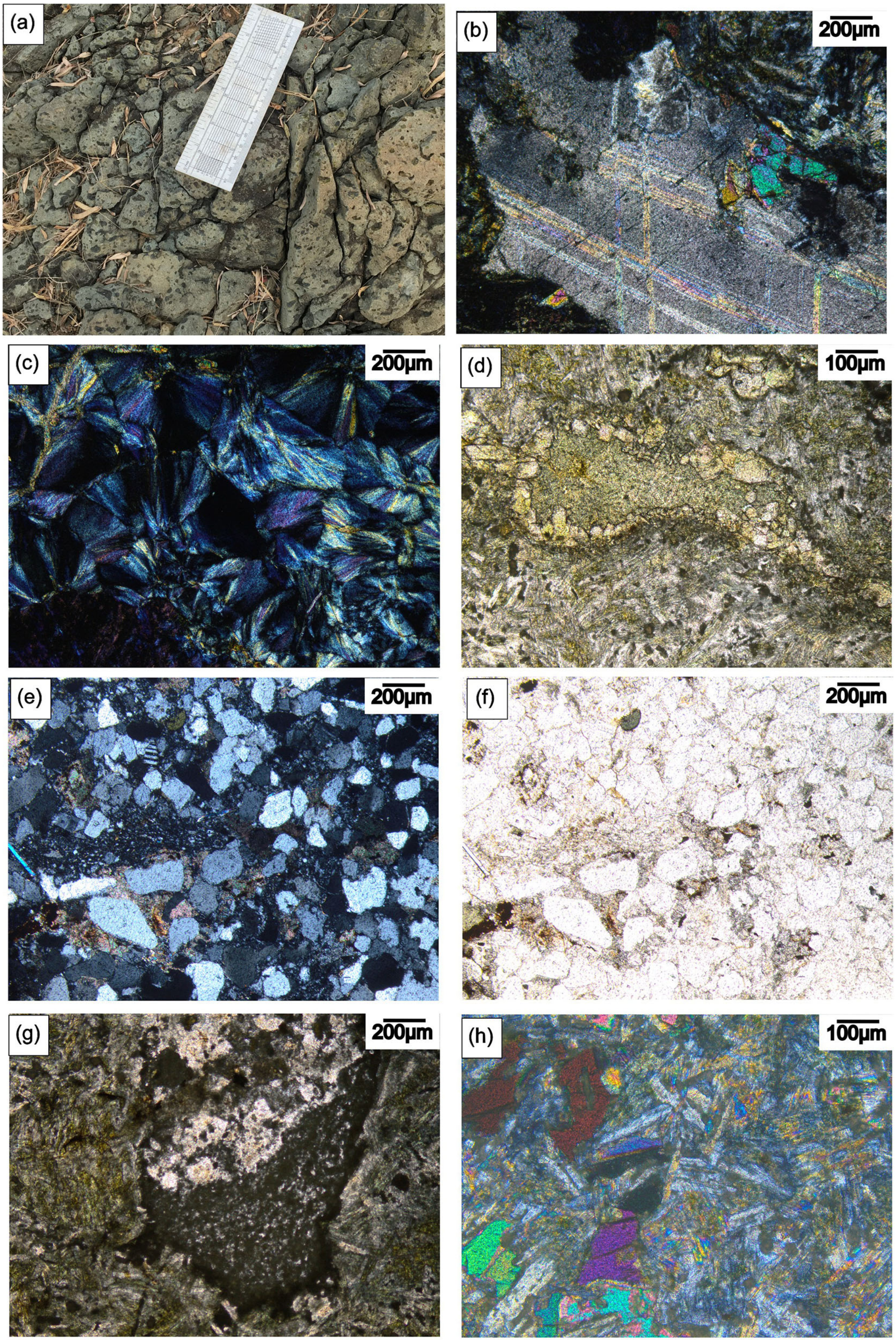

Figure 5. (**a**) Amalgamated thick bedded greenish, chloritized pyroclastic lava flow deposit from the Kair section; note abundant presence of lithic crystals, and green to black lapilli in the groundmass, chloritized and partially devitrified glass fragment, vug-filling secondary minerals like calcite (**b**) and zeolites (**c**) inward growth of crystal (calcite) within the vugs (**d**), presence of angular clastics with grain interspaces occupied by chloritized lava (**e** = cross-polarized, **f** = plane polarized), droplet-shaped pumice fragment (**g**) and sub-porphyritic texture defined by plagioclase microlaths, glass and microlites (**h**).

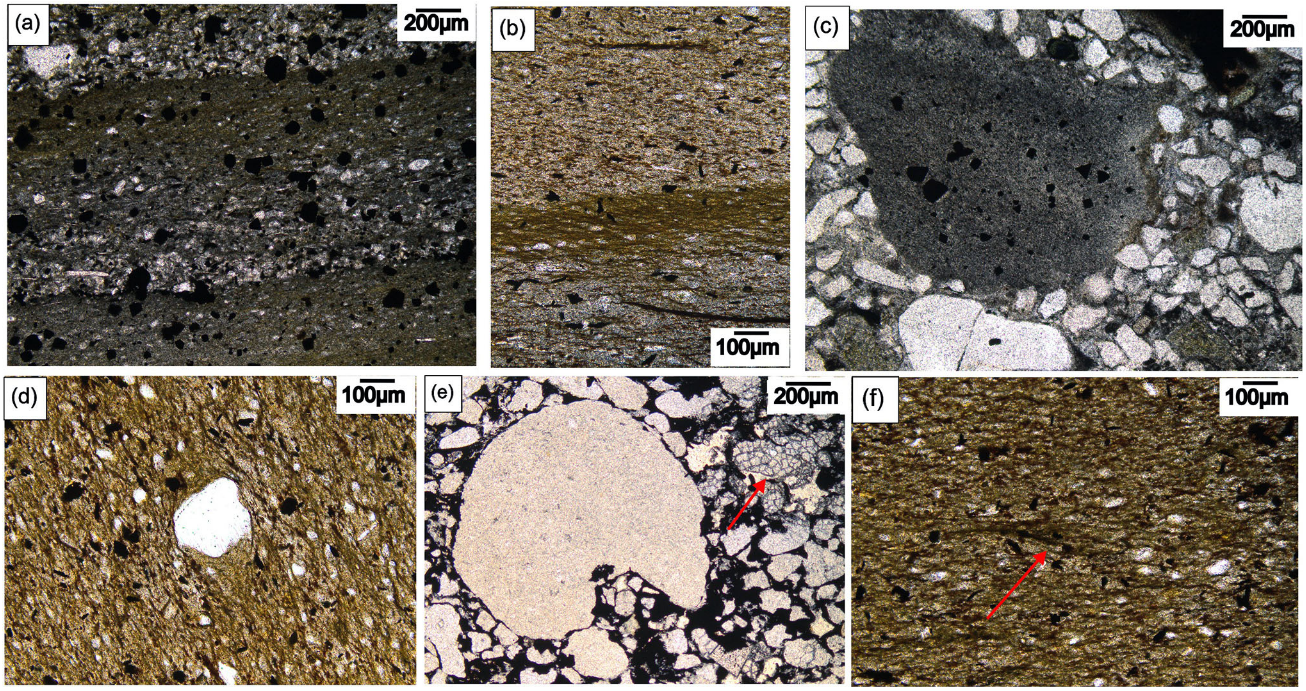

Figure 6. Welded tuff with crystals, pyroclasts and angular vitroclasts (**a**), Fiamme; irregular, elongated dark glassy lenses formed by welding of juvenile pumice clasts (**b**), welding of clastics with vitroclast along its boundary (**c**), fibrous, striated fiamme wrap around crystal (**d**), indicating extreme degree of welding, shattered blob-shaped quartz (arrowed) and embayed quartz (**e**) and pyroclastic fragment with bow-tie shape (**f**).

medium- to coarse-grained sandstone (figure 4b; lithofacies SS 2, table 2), deposits of this lithofacies are best exposed near the Hathori village (figures 1b, 2), though counterparts of this unit are also tracked at the outskirt of Kair village. The maximum recorded thickness is 5 m and documented from the Hathori section either as a massive unit or as a well-laminated unit having mm- to cm-thick laminations (figure 4c), traced laterally over 0.5 km. Laminations though commonly horizontal (figure 4c), evidence of warping and syndepositional deformation are not uncommon. In some cases, intercalation by poorly sorted, granular/pebbly pyroclastic surge flows and tuffaceous breccia can also be noticed (figure 4d and e). In the hand specimen, the tuff unit is extremely fine-grained (mostly below 20 μm in size), buff or dark greenish-grey in colour, and splintery with razor-sharp edges in broken pieces. In thin section, the tuff unit is composed of elongated grey to black fiamme (flattened pumice lenticles), crystal (quartz and plagioclase), pyroclasts (100–150 μm), and angular vitroclasts (50–100 μm) (figure 6a–c). Fiamme is elongated, 0.1–0.5 mm long, with a length-to-thickness ratio varying from 10:1 to 100:1. Internally fiamme are fibrous or striated in texture, wrap around crystals and volcanic clasts, orient parallel to clast elongation, and are identified as compact tube vesicle structures with extreme degrees of welding and crystallization (figure 6d). Also seen are high-temperature plastic deformation and welding of glass shards with collapsed vesicles. Vitroclasts are dominantly microlitic, altered to sericite and chlorite, and often pyrite-bearing. Ovoid shaped quartz crystals are at times shattered and with embayed boundaries (figure 6e).

In the Kair village area, the tuff unit is encased between basalt at the top and shallow marine sandstone-shale at the base of the exposed succession (figure 2). Intervened by cm-thick fine sandstone interbeds, the best-developed tuff unit measures 35 cm in thickness. Pumice clasts in the tuff are sub-angular to sub-rounded, flattened pyroclastic fragments and shards are bow-tie shaped (figure 6f), with thread-like terminations; often altered/devitrified to sericite, chlorite, and opaque oxide. Majority of fiamme is altered to micro-quartz and feldspar with an opaque oxide rim and internally fibrous with wispy termination.

Interpretation: The presence of fiamme has been established as a criterion for recognizing welding in pyroclastic facies, both in form of pyroclastic flow (Sparks *et al.* 1973; Freundt *et al.* 2010) and fall

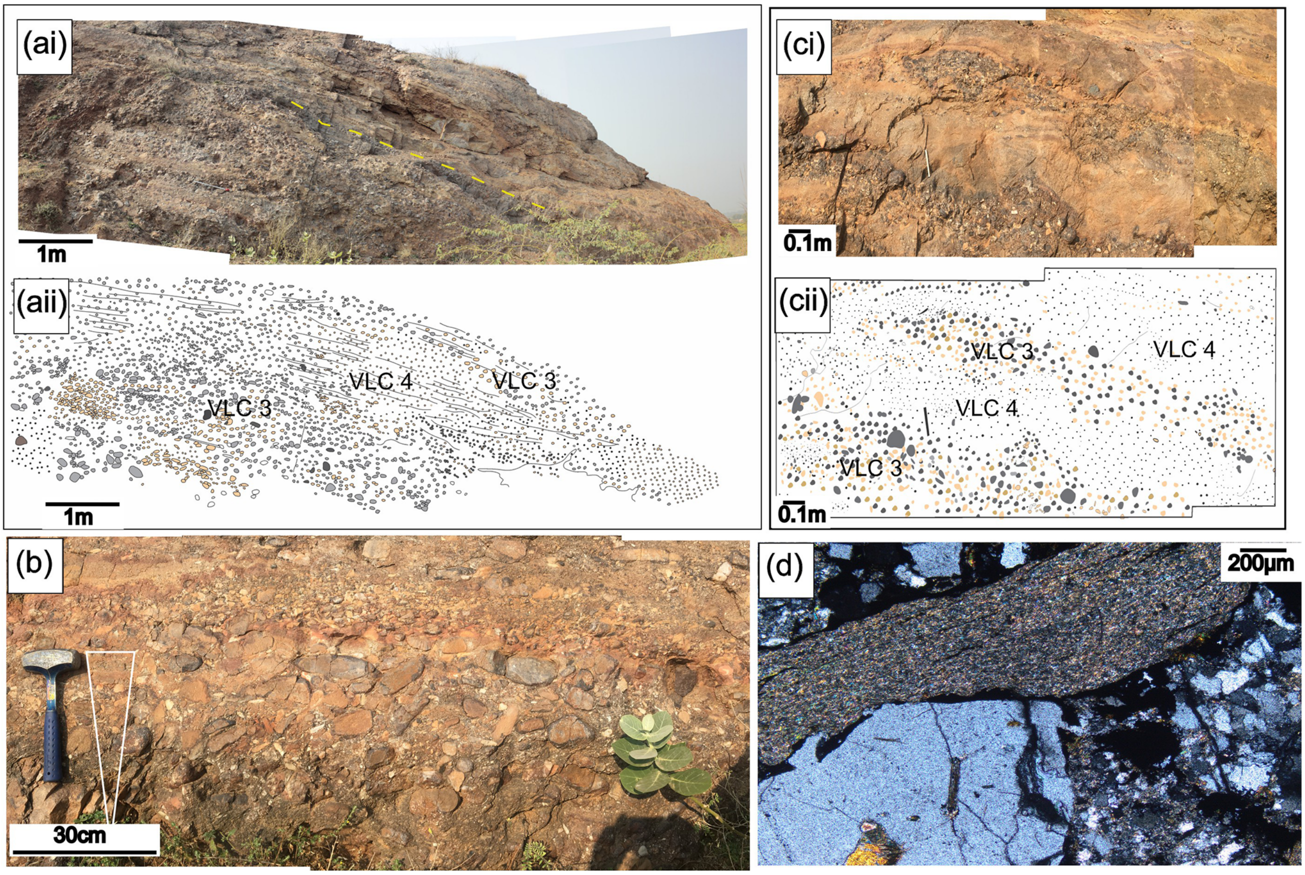

Figure 7. Field photograph (**ai**) and sketch (**aii**) of bouldery pyroclastic density flow deposit exposed at the Nithar section; deposit of PDC with flow boundary zone dominated by granular flow regime, operation of kinematic squeezing and kinetic sieving (**b**), also notice alteration between bouldery and granular layer with sharp contact; alternation of pyroclastic fall deposit with thin-bedded PDC (**ci**) and sketch thereof (**cii**); vesicular pumice clast with thin rim of sericite and opaque oxide (**d**).

(Wolff and Wright 1981; Bull and McPhie 2007). The occurrence of fiamme in both Hathori and Kair tuff bears indication of welding within the tuff unit. Glassy juvenile fragments such as bubble-wall glass or pumice fragments, sinter, anneal, or weld in point or surface contact either through syn-depositional agglutination in presence of water (Branney and Kokelaar 1992; Grunder and Russel 2005) or by mechanical compaction in course of burial (Grunder *et al.* 2005). However, mechanically compacted, and flattened clasts normally do not show viscous tubular structures under the microscope as demonstrated by syn-depositional welded compacted pumice clasts (Kokelaar and Busby 1992). Flattening and attenuation of shards and pumice fragments around quartz and feldspar clasts, as observed in the present case, bear tell-tale evidence for viscous attenuated flowage under syn-depositional welding. In some cases, heterogeneous alteration of pyroclasts also resulted in alternation between attenuated portions with unaltered portions retaining the original structure. Solution seams, mostly restricted where pumice clasts are not altered, represent portions with ductile deformation, subsequently replaced by a zeolite group of minerals. A subaqueous origin for the welded tuff unit is argued from (i) the shallow-marine origin of associated sedimentary strata with undoubted wave influence, (ii) occurrence of rip-up angular shale clasts, and (iii) presence of pumice clasts with elongated streaked/fibrous textured fiamme.

4.2 *Secondary volcaniclastic deposit*

4.2.1 *Subaerial deposits*

Secondary volcaniclastic deposits are interbedded with basalt and sandstone-siltstone units and interpreted as subaerial deposit.

4.2.1.1 *VLC 3: Pyroclastic debris current (PDC) deposit:* Among different kinds of volcaniclastic processes reported in the literature, pyroclastic density currents (PDC) represent one of the most

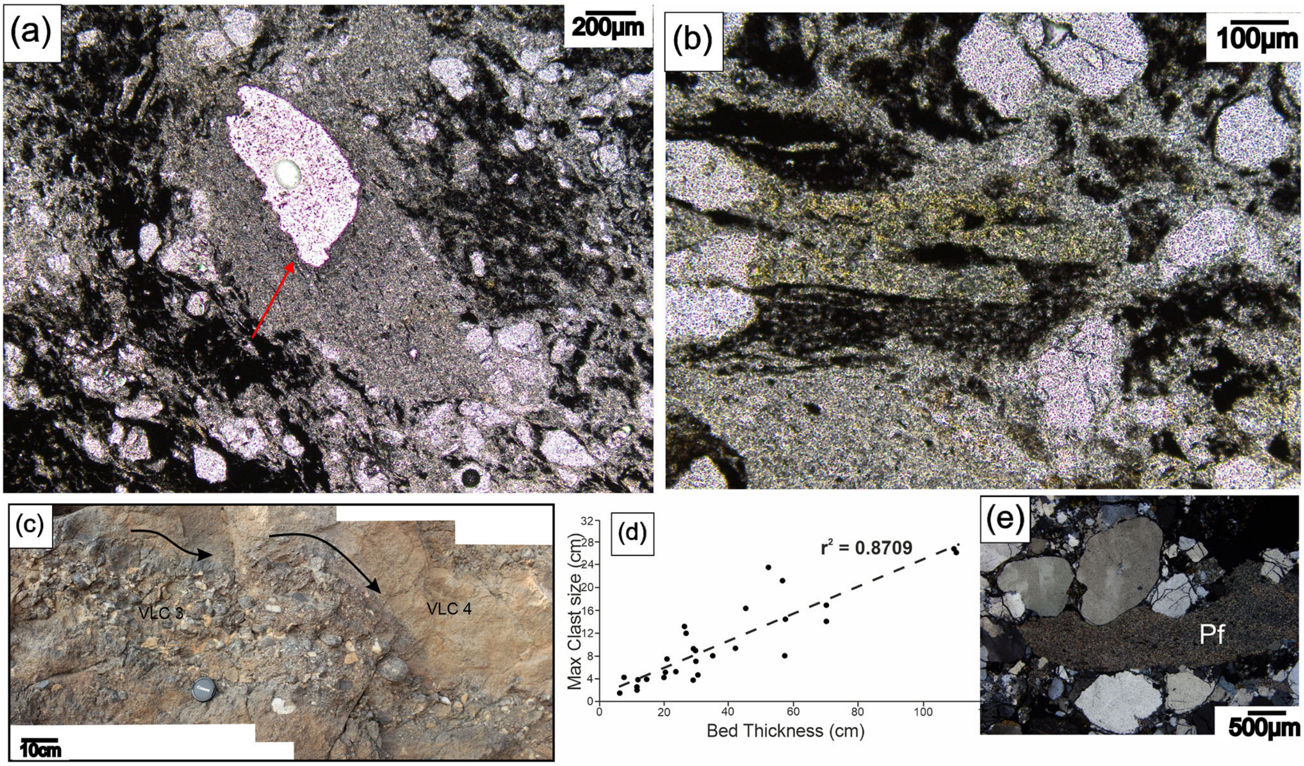

Figure 8. Relict tube vesicle within pyroclastic fragment (arrowed) (**a**); pyroclastic fragment altered to sericite, chlorite and opaque oxide (**b**); and smaller clasts swirling around the larger clasts in the flow direction (**c**); binary plot involving clast size and bed thickness from the PDC beds; note a strong correlation ($r^2 = 0.87$) between the two variables (**d**); and annealing of clastic grains (quartz, feldspar) along the margin of pyroclastic fragments (Pf) (**e**).

complex and spectacular ones associated with explosive volcanic eruptions (Sparks 1976; Fisher 1979; Druitt 1998; Calder *et al.* 1999; Denlinger and Iverson 2001; Branney and Kokelaar 2002; Dellino *et al.* 2010; Brown and Branney 2013; Sulpizo *et al.* 2014, and many others). As dense multi-phase gravity currents, constituted of pyroclastic particles and gas in various degrees of concentration and mixing, PDCs move across any landscape under the action of gravity either in the form of fluid-dominated flow, solid-dominated flow, or a continuum between the two.

Description: In the present study, the best exposures of the PDC deposits are observed near the Nithar village, wherein a ∼35 m thick outcrop (figure 7a), overlying medium to coarse-grained planar or trough cross-stratified reddish-coloured arkosic sandstone (lithofacies SS 1; table 2), exposes a unique opportunity for documentation of deposit character and flow rheology. Paleocurrent measurement from the associated sandstone reveals a dominant northeastward paleoflow (figure 2). In alternation with pyroclastic fall (coarse and fine-grained; VLC 4, discussed later) deposits, PDC units are present with varying grain size and internal structure and are described based on the degree of sorting, clast size, massiveness/nature of grading (normal, reverse), and lateral as well as a vertical relationship with adjoining strata. A careful look into the exposure allowed the identification of four different types of PDC deposits of varying flow competence, steadiness, and depositional style. It may be worth mentioning here that the bedding geometry and sorting character of PDC deposits essentially represent depositional processes and to a lesser extent the transport processes in the entire flow.

Either as a massive unit or with grading (normal and inverse), laterally heterogeneous bouldery and pebbly (block and bomb; >64 mm) conglomerates with varying degrees of clast concentration, represent this facies (figure 7a–c; table 2). The thickness of these units varies between 12 and 60 cm (the average thickness being 38 cm); in some cases, isolated trains of block/bomb sized fragments represent the facies unit. In thicker beds, the lateral changeover is recorded in tens of meter exposure scale from massive conglomerates with chaotic fragments to conglomerates with fragment size and concentration grading. Poorly sorted, subrounded

Table 3. *Bed thickness (BTh) vs. maximum clast size (MPS) for the VLC 3 facies of Nithar section (r^2= 0.87).*

Bed thickness (cm)	Max clast size (cm)
30	9
15	4
30	7
70	17
27	12
70	14
35	8
109	27
57	21
45	16
52	24
30	9
110	26
27	13
58	14
21	8
21	5
20	4
42	9
7	1
57	8
24	5
8	4
12	4
12	3
29	4
31	5
12	2

to rounded block- and bomb-sized fragments of pyroclast, basalt, sandstone, and vein quartz, in decreasing order abundance, represent the clast population with matrix in interclast areas composed of sandy to granular lithic (pyroclastic lapilli, basalt, sandstone), crystal (feldspar, quartz) and glassy (pumice) fragments. Blocky tube pumice fragment with vesicles is rimmed by thin sericite + opaque oxide film (figure 7d). In some cases, relict tube vesicles are visible within pyroclastic fragments (figure 8a). Annealing of clastic grains (quartz, feldspar) along the margin of pyroclastic fragments observed at cases (figure 8e). Most of the pumice fragments are sub-angular to angular (figures 7b and 8a). Flattened pyroclastic fragments are often found altered/devitrified to sericite + chlorite + opaque oxide (figures 7d and 8b). In general, elongated triaxial ellipsoid and near ovoid are the preferred fragment geometry (figure 7b and c). Fragment size ranges from 10 m to 20 cm; the average clast size is 15 cm. In a single bed with inverse concentration grading, fragments are elongated, bed-parallel, and in contact with each other at the upper part forming a mesh, whereas fragments in the lower part of the bed are isolated, surrounded by matrix, and oriented at moderate to high angle with the bedding plane (figure 7b and c). At times, the distribution of smaller fragments in the matrix is controlled by the shape and orientation of larger fragments; smaller clasts either swirl around or slide down the surfaces of larger clasts (figure 8c). Elongate fragments are commonly oriented parallel to the bedding plane or imbricated. With sharp, non-erosional contacts, VLC 4 (pyroclastic fall) facies units (discussed later) overlie the conglomerate beds in succession (figure 7ai and aii) and thereby resulting in fining-upward depositional cycles. Basal contacts of conglomerate units are either sharp, planar, and non-erosional or rugged with blocks/bombs of the conglomerate units protruding within the underlying VLC 4 layers. Similarly, the upper contacts of conglomerate beds are commonly rugged recording infiltration of VLC 4 sediments between the blocks and bombs at the upper part of conglomerate beds. Measurement of maximum clast size and corresponding bed thickness reveals (i) a good positive correlation between the two ($r^2 = 0.87$) (figure 8d) and (ii) 1.5–5 times greater bed thicknesses in comparison to maximum clast sizes (table 3). Upward in the section, the thickness of this facies unit decreases at the expense of VLC 4 facies units.

Interpretation: Matrix-/clast-supported massive, normal- or inverse-graded conglomerates, with block- and bomb-sized volcanic/lithic clasts, and pyroclastic matrix, are identified as products of PDCs in which large-sized fragment entrainment and segregation are dominated either by matrix strength or by granular flow (Fisher 1979, 1984; Branney and Kokelaar 2002). A debris flow origin with plastic to turbulent flow character is surmised from the non-erosional-based massive to the erosional-based graded character of these deposits. Although debris flows are laminar, still turbulence may develop in such flows even without the addition of ambient water (Fisher 1984; Manville *et al.* 2009). Despite high concentration, turbulence generates within such flows because of high velocity (body transformation; Hampton 1972) leading to an increase in the Reynold number ($\rho Ud/\mu$) over Bingham number ($d/\mu U$) (where U is the average velocity, d is the thickness of the flow, ρ is the density of the flow, μ is the viscosity of the flow) (Middleton 1970; Fisher 1984). Within meters-scale exposure width, a transformation in the conglomerate body from a massive and chaotic fragment distribution character to an inverse-graded character bears testimony to this fact. Whereas poor sorting and chaotic clast distribution signify the role of matrix strength in the flow, in granular flows depending on clast concentration the entrainment mechanism varied; in flows with high clast concentration, particle–particle interactions dominated the transport mechanism and clast entrainment. In contrast, domination of turbulence in flows with low to moderate clast concentration resulted in normal concentration grading of clasts; flow shear rate, rate of deposition, and concentration mutually controlled the sediment dispersal pattern and depositional regime in the flow (Charbonnier and Gertisseir 2011; Brown and Branney 2013; Sulpizio *et al.* 2014). The ambient high temperature caused the inflation in granular mass and pressure generated thereby is termed as dispersive pressure (Bagnold 1954). Whereas at high temperature the dispersive pressure keeps the granular mass in a liquified state, the inflation in such mass promotes particle segregation through kinetic sieving. A combined process involving trickling down of smaller particles through the inter-clast voids and preferentially migration of larger clasts towards the flow upper boundary by the kinematic squeezing result in reverse grading within such flows; a frequent collision of larger clasts helps in the process of self-sustenance and kinematic squeezing (Le Roux 2003; Chakraborty *et al.* 2009). The bed-parallel orientation of clasts in contact with each other in the upper part of the conglomerate bed bears an indication of strong shear in the top part of the flow. Isolated clasts at the lower part of the bed with a high angle to the bedding are elutriated under high fluid (gas) pressure. From 1.5–5 times higher bed thickness in comparison to maximum fragment size, a subaerial character is inferred for the PDC units (cf. Gloppen and Steel 1981). Roundness in volcanic clasts, observed at cases, may be the result of syn-volcanic transport on volcanic slopes, as documented from silicic pyroclastic units in Dongargarh Igneous Province, Bastar Craton, India (Sensharma and Gaur 2022). Association with moderate- to poorly-sorted cross-stratified arkosic sandstone of alluvial origin corroborates the contention. Further, from a positive correlation between clast size and bed thickness of mass flows ($r^2 = 0.87$; figure 8d), an increase in eruptive discharge with the increase in flow competence is inferred (Nemec and Steel 1984; Barkat *et al.* 2020). Any significant erosion of mass flow beds is ruled out from the positive correlation coefficient and the intersection of the regression line with the maximum clast size axis holds an indication for the operation of individual cohesive flows without much post-depositional modification of bed thickness (Miall 1970; Nemec and Steel 1984; Shultz 1984; Köykkä 2011). In this context the clast annealing along the boundary of pyroclast grains, observed under microscope, is identified as the result of vitreous rheology of pyroclasts; their degassing, compaction and quenching in high temperature, high pressure diagenetic environment (cf. Gifkins *et al.* 2005; Li *et al.* 2022).

4.2.1.2 *VLC 4: Pyroclastic fall deposits*

Description: This facies type is well exposed at Nithar and Hathori village sections and characterized by tabular/broad lenticular thin (≤ 6 cm in thickness) beds of granular (with strewn pebbles) rusty to reddish coloured deposit (VLC 4a) in alternation with very fine-grained yellowish ash deposit (VLC 4b). At the Nithar section occurrence of the facies is noticed in alternation with the VLC 3 facies units with sharp to gradational contacts (figure 9a). The counterpart of this facies is also noticed at the basal part of the Hathori section where decimeter-thick beds of VLC 4b and isolated beds of VLC 4a are noticed in alternation with trough-cross-stratified granular alluvial sandstone (figures 2 and 9b, c). Upward at the Hathori section, thin beds of VLC 4b are recorded in alternation with heterolithic assemblage of fine sandstone and shale that bears undoubted signatures of wave action (figure 9d). Internally, the VLC 4a units are either massive or with normal concentration grading but without any cross-bedding or gas escape structure. Bases of these beds are commonly uneven with boulders and pebbles from the underlying VLC 3 facies unit often found protruding within the overlying strata. Contacts between VLC 4a facies and overlying facies VLC 4b are abrupt and ungraded. Under the microscope observation, samples from facies VLC 4a are reddish/rusty in colour and constituted of lithic fragments, crystals, glass shards, pumice, and iron oxides (12–15%) in variable proportion and with poor sorting. Accretionary (armoured) lapilli with aggregates agglomerated around coarse ash particles is a common observation (figure 9e). Grain size analysis revealed mean grain size 1.11 mm though at times the occurrence of isolated pebble-sized clasts is not uncommon. Alike VLC 3 PDCs, pyroclasts in these facies show a dominant rounded to ovoid clast geometry; their short axis diameters range in size from 18 to 42 mm.

Interpretation: Plane parallel beds in this type of deposit mantling the underlying relief bear tell-tale evidence in favour of pyroclastic fall deposition. In addition, the features including (i) sharp bedding planes dividing units with contrasting grain sizes, (ii) incipient normal grading within coarse-grained units, and (iii) absence of any unidirectional bedding feature such as mega-ripple, confirm the interpretation that the facies unit is a product of pyroclastic fall from a spasmodic, non-sustained eruption with many short-lived pulses. Coarse grain size, poor grading, lack of internal structure, and lack of basal scour in VLC 4a suggest the operation of high-concentration pyroclastic fall. Rapid settlement may result in coarse-grained, massive, normal-graded character without any internal structure (Cousineau 1994). Similar grain size oscillations, reported from Plinian deposits, are identified as a product of partial column collapses whereby mass is partitioned between the convecting and collapsing region (Houghton and Carey 2015). Though less in abundance in comparison to PDCs, documentation of undoubted signatures of welding between individual pyroclasts within these facies types allows us to infer retention of heat in individual clasts in course of flight and subsequent rapid burial and loading with the accumulation of overlying tephra. Additionally, the rusty/reddish colour with alteration of iron oxide minerals, as evident under a microscope, also supports the colouration of the facies under a high-temperature thermal effect.

5. Geochemistry

To understand the nature of magmatic input in the course of Bayana sedimentation in a holistic manner, the present study took into its purview geochemical analyses from a total of seventeen samples, out of which ten samples were collected

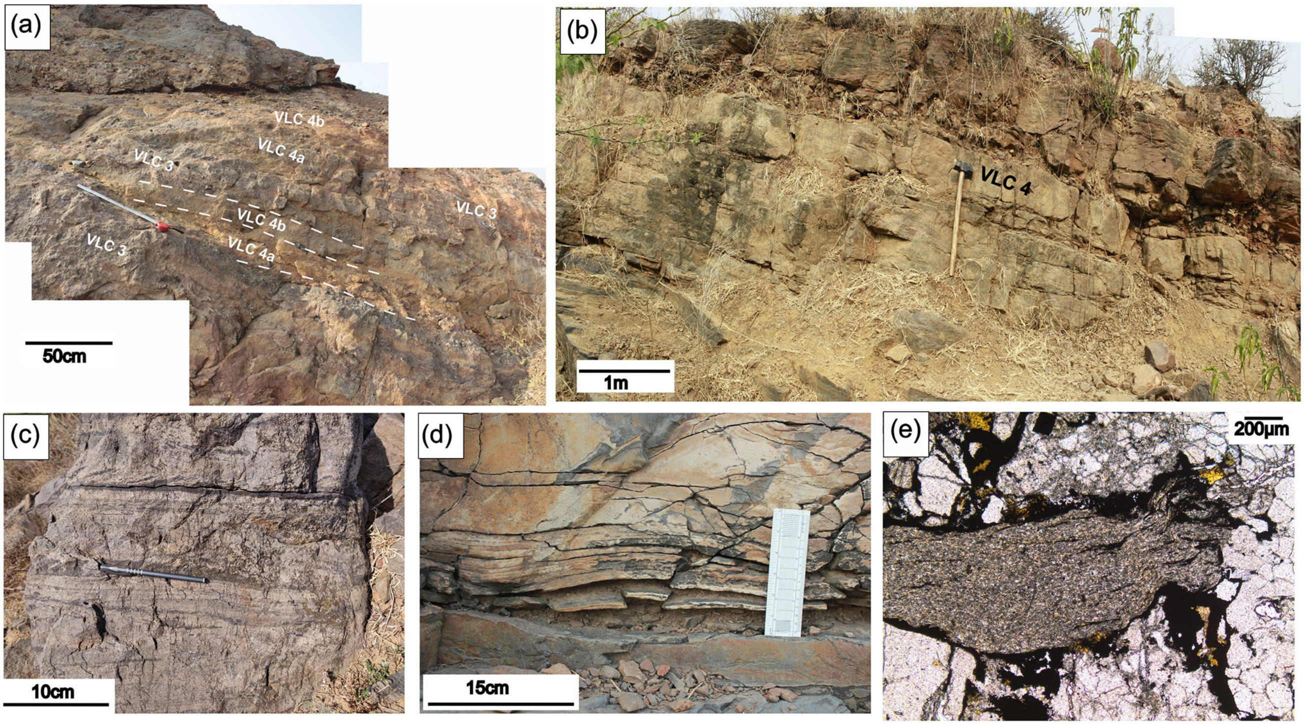

Figure 9. Field photograph illustrating alternation between PDC unit (VLC 3) and pyroclastic fall (VLC 4a,b) deposit at the Nithar section (**a**); Decimeter-thick bed of VLC 4 (shown by hammer head) in alternation with granular alluvial sandstone at the Hathori section (**b**); Plane-laminated and trough cross-stratified alluvial poorly-sorted sandstone at the Hathori section (**c**); Thin beds of VLC 4b in alternation with heterolithic fine sandstone-shale succession in the upper part of Hathori section with undoubted wave signature (**d**); and accretionary armoured lapillae with delicate feathery terminations, having a brush-like highly compacted end (**e**).

from variants of volcaniclastics described under the present study and seven analyses of mafic volcanic rocks, collated from the work of Raza *et al.* (2007) (table 1). Since the volcaniclastics are heterogeneous in character care was taken for geochemical sampling. Samples from matrix part of PDC conglomerates (NT1, 2) are collected for geochemistry. Other samples (KR1–3, KR4 and HT1–4) are either from ignimbrite (VLC 1) or from tuff layers (VLC 2, VLC 4) and hence, bulk analysis was carried out for geochemical characterization Though most of the analyzed volcaniclastic samples record total oxide + loss on ignition (LOI) values close to 100, it is worth mentioning here that the sample NT1, despite repeat analysis, records a total value of 88.592 (major oxides + LOI) only.

5.1 *Major oxide*

A wide variation in the SiO_2 and Al_2O_3 contents (51.8–85.01 wt.%, average 62.55 wt.% and 3.42–18.67 wt.%, average 12.66 wt.%, respectively) is documented from the Bayana volcaniclastics in contrast to a narrow range of SiO_2 (50.13–52.75 wt.%, average 50.98 wt.%) and Al_2O_3 (9.88–14.84 wt.%, average 11.18 wt.%) values reported from the volcanic rocks (table 1). Except for sample no. NT1 (collected from VLC 3), most of the volcaniclastic samples record total oxide contents close to 100 (table 1) and hence, considered as primary compositional values. TiO_2 (0.52–1.43 wt.%, average 1.01 wt.%) and MnO (0.01–0.35 wt.%, average 1.12 wt.%) contents are low in the volcaniclastics and in the volcanic rocks (TiO_2 = 1.06–1.96 wt.%, average 1.47 wt.% and MnO = 0.19–0.23 wt.%, average 0.21 wt.%). Except for samples from pyroclastic flow (KR1–3), volcaniclastics, in general, record low MgO content (0.13–2.36 wt.%, average 1.51 wt.%), in contrast to high MgO values (7.03–11.02 wt.%, average 9.27 wt.%) in the volcanic rocks. Mg number ranges from 4.14 to 63.28, in which Mg number for some volcanoclastic samples ranges between 4.14 and 30.58, and Mg numbers for volcanic rocks and pyroclastic lava samples (KR1–3) range between 49.92 and 63.28. Amongst all samples of volcanic rocks and volcaniclastics, pyroclastic flow samples (KR1–3) and volcanic rocks samples (BY1–BY5) record high CaO (7.02–8.84 wt.%, average 7.74 wt.% for pyroclastic flow samples and 7.08–10.47 wt.%, average 8.27 wt.% for volcanic rocks samples) and Na_2O (3.76–4.45 wt.%, average 4.04 wt.% for pyroclastic flow and 1.28–2.14 wt.%, average 1.70 wt.% for volcanic rocks samples) values. K_2O contents in many volcaniclastic samples are relatively high and with wide-ranging values (1–7.97 wt.%, average 4.00 wt.%) in comparison to low, restrictive values in volcanic rocks (0.52–1.86 wt.%, average 1.02 wt.%). From the total alkali *vs.* silica (TAS) plot, it is inferred that the composition of volcanic rocks in the Jahaj–Govindpura Formation falls dominantly under the basalt field, whereas volcaniclastic samples cover a wide range of compositions varying between trachybasalt, trachyandesite, basaltic andesite, and rhyolite. A similar trend is also noted in the K_2O–SiO_2 plot (Peccerillo and Taylor 1976) (figure 10a). Since potassium and sodium are highly mobile elements in the course of weathering and burial of volcaniclastic sediment, the K_2O–SiO_2 and total alkali (Na_2O + K_2O) *vs.* SiO_2 plots display significant scatter in the data and hence, we reserve our comment regarding the characterization of magma clan based on these plots (figure 10b). In the AFM diagram, both volcanic rocks and volcaniclastics, except the samples from pyroclastic flow (KR1–3), fall in the tholeiite field; pyroclastic flow samples plot in the calc-alkaline series (figure 10c). In the Fe + Ti–Al–Mg plot of Jensen (1976), samples dominantly plot in the high-Fe tholeiitic basalt field (figure 10d). The major element geochemistry provides a general impression that the volcanic rocks and magmatic clan of volcaniclastic rocks consisted of both tholeiitic and calc-alkaline/silicic composition. In this backdrop, a general high K-content in volcaniclastics is a mismatch and hence, K/Ca ratio of volcanics and volcaniclastics were calculated separately to understand any effect of secondary alteration under diagenesis. A consistent high K/Ca ratio (av. 63.90; table 4) in volcaniclastics support secondary diagenetic alteration (cf. Chambers *et al.* 2004).

5.2 *Trace element and rare earth element (REE)*

Since in the literature, all trace element data are not available for the volcanic rock samples, we restrain from any comparison between volcanic rocks and volcaniclastics in terms of trace element composition and limit our discussion to the volcaniclastics only. In trace element composition volcaniclastic samples record widely variable characters. High values of Cr, Sr, and very high

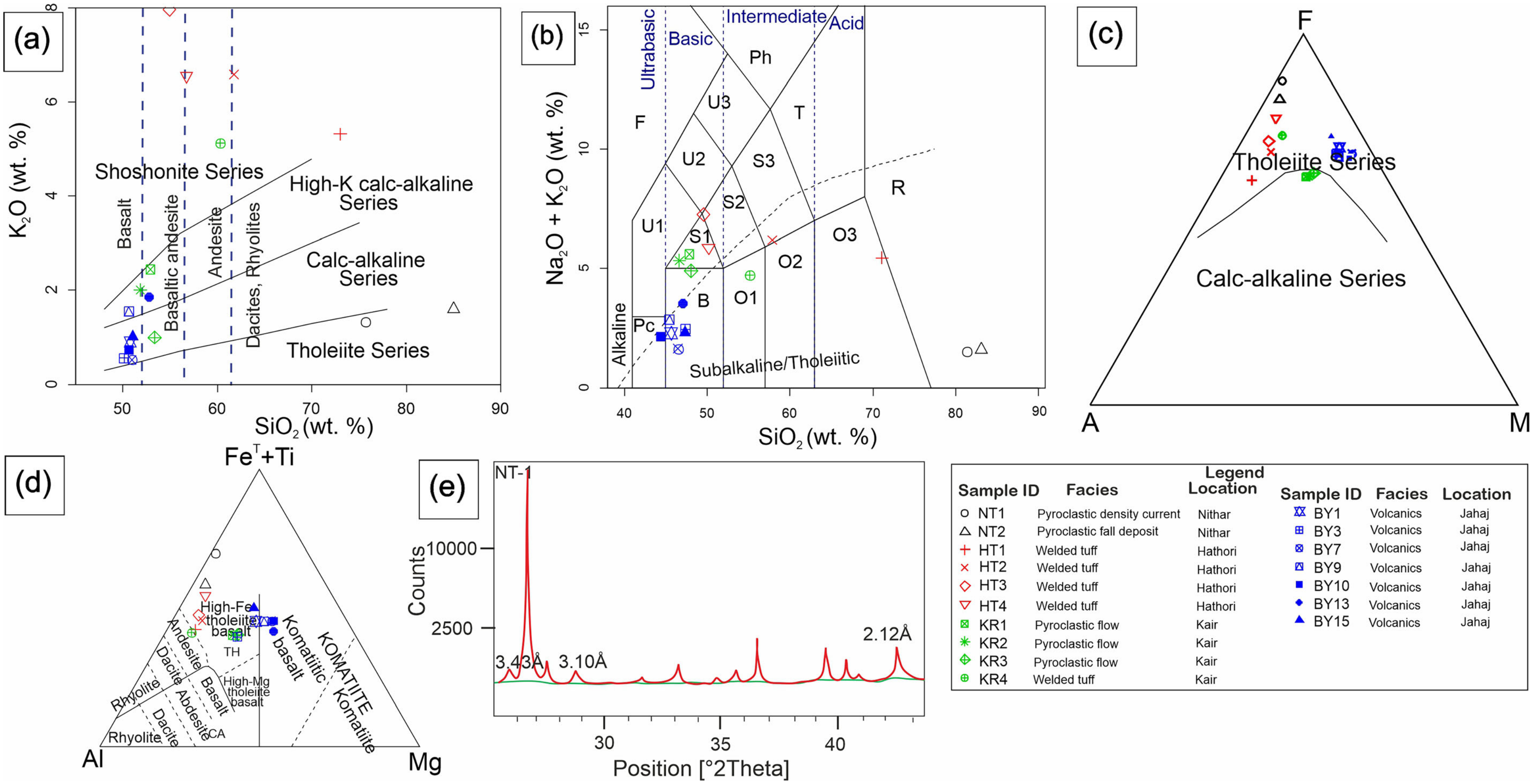

Figure 10. Geochemical plots: K_2O–SiO_2 (after Peccerillo and Taylor 1976) (**a**) and total alkali-silica (after Le Bas *et al.* 1986) (**b**); diagrams showing composition of Bayana volcaniclastics; Alkali (a)–Iron (F)–Magnesium (M) ternary AFM diagram illustrating tholeiitic to calc-alkaline affinity for volcaniclastics (**c**); Fe + Ti–Al–Mg plot (after Jensen 1976) illustrating high-Mg tholeiitic character (**d**); X-ray diffraction data from sample NT1 showing the presence of high Ba containing mineral Celsian (**e**). Abbreviations for figure **b**: Pc: picrobasalt, B: basalt, O1: basaltic andesite, O2: andesite, O3: dacite, R: rhyolite, S1: trachybasalt, S2: basaltic trachyandesite, S3: trachyandesite, T: trachyite, U1: tephrite, U2: phonotephrite, U3: tephriphonolite, Ph: phonolite, F: foidite.

Table 4. *K/Ca ratio for Volcaniclastics and volcanics samples of Jahaj–Govindpura volcanics (JGV) Formation.*

Sample ID	Lithology	K/Ca ratio
Volcaniclastics		
NT1	Pyroclastic density current (VLC 3)	59.34
NT2	Pyroclastic density current (VLC 3)	53.51
HT1	Pyroclastic fall (VLC 4)	5.04
HT2	Pyroclastic fall (VLC 4)	14.09
HT3	Pyroclastic fall (VLC 4)	140.2
HT4	Welded tuff (VLC 2)	133.47
KR4	Welded tuff (VLC 2)	41.62
Ignimbrite and volcanics		
KR1	Pyroclastic flow (VLC 1)	0.21
KR2	Pyroclastic flow (VLC 1)	0.13
KR3	Pyroclastic flow (VLC 1)	0.08
BY1	Volcanics	0.12
BY5	Volcanics	0.09
BY7	Volcanics	0.08
BY9	Volcanics	0.23
BY10	Volcanics	0.08
BY11	Volcanics	0.28
BY13	Volcanics	0.14

values of Ba are recorded in sample NT-1 (bouldery pyroclastic conglomerate). Besides NT-1 which yields an abnormally high Ba value (20882 ppm), volcaniclastics, in general, record high Ba content (178–1806 ppm). X-ray diffraction (XRD) study of this sample reveals the presence of Ba-K bearing feldspar, celsian in the system (figure 10e). Nearly all volcaniclastic samples record high Cr values (178–746 ppm). Whereas Sr contents are relatively high (113–129 ppm) in pyroclastic flow samples (KR1–3), Rb contents (102–294 ppm) are high in welded tuff (HT1–4 and KR4) samples. Relatively high (106–172 ppm) Zr contents are recorded in most of the volcaniclastic samples except in pyroclastic flow samples (KR1–3). Since incompatible high-field strength elements such as Ti, Nb, Y, Zr, and Hf remain largely immobile in low-temperature alteration processes, the elements are given priority in the characterization of the magma. In Nb/Y *vs.* Zr/TiO_2 plot (Winchester and Floyd 1977) from volcanic rocks and pyroclastic lava flow samples (KR1–3) suggest a sub-alkaline basalt character whereas welded tuff samples (HT1–4) dominantly fall along the boundary between alkali basalt and trachy-andesite (figure 11a). In Nb/Yb *vs.* Th/Yb plot (Pearce 2008), all analyzed samples (including both volcaniclastics and volcanic rocks) plot in the volcanic arc array, which is also corroborated in the La/Yb *vs.* Th/Nb plot where the samples fall in the fields of alkaline arcs, and marginally in the continental arcs field (figure 11b and c). Relative Nb depletion allowed us to interpret the magma clan as typical island arc tholeiites (cf. Hiscott and Gill 1992) (figure 11d).

In general, Bayana volcaniclastic rock samples are characterized by enrichment in large ion lithophile elements (LIL; Rb, Ba, and Th) in comparison to high field strength elements (HFSE; Nb, Zr, and Y). In addition, the Th/Sc ratio is identified as a good proxy for the understanding of original melt composition (Taylor and McLennan 1985; Cullers *et al.* 1988; McLennan and Taylor 1991; McLennan and Hemming 1992; Condie 1993; Xiang *et al.* 2015). The upper continental crust comprised of mature igneous, metamorphic, and sedimentary rocks displays a Th/Sc ratio of ∼1 (0.97). In contrast, Th/Sc ratio from the undifferentiated volcanic arc is <0.02. A classification scheme for volcaniclastic sediments based on Th/Sc ratio includes a value of ratio <0.1 in mafic rocks, 0.1–0.8 in intermediate rocks, and more than 0.8 in felsic rocks (Taylor and McLennan 1985; Condie 1993). Leaving aside the pyroclastic lava samples, the Bayana volcaniclastic samples, on average, record a Th/Sc ratio of 0.40; the pyroclastic flow samples (KR-1, 2, 3) record an average value of 0.04. The majority of the volcaniclastic samples record Th/Sc values between 0.1 and 0.8 and hence, indicate an intermediate composition, whereas pyroclastic flow samples with an average

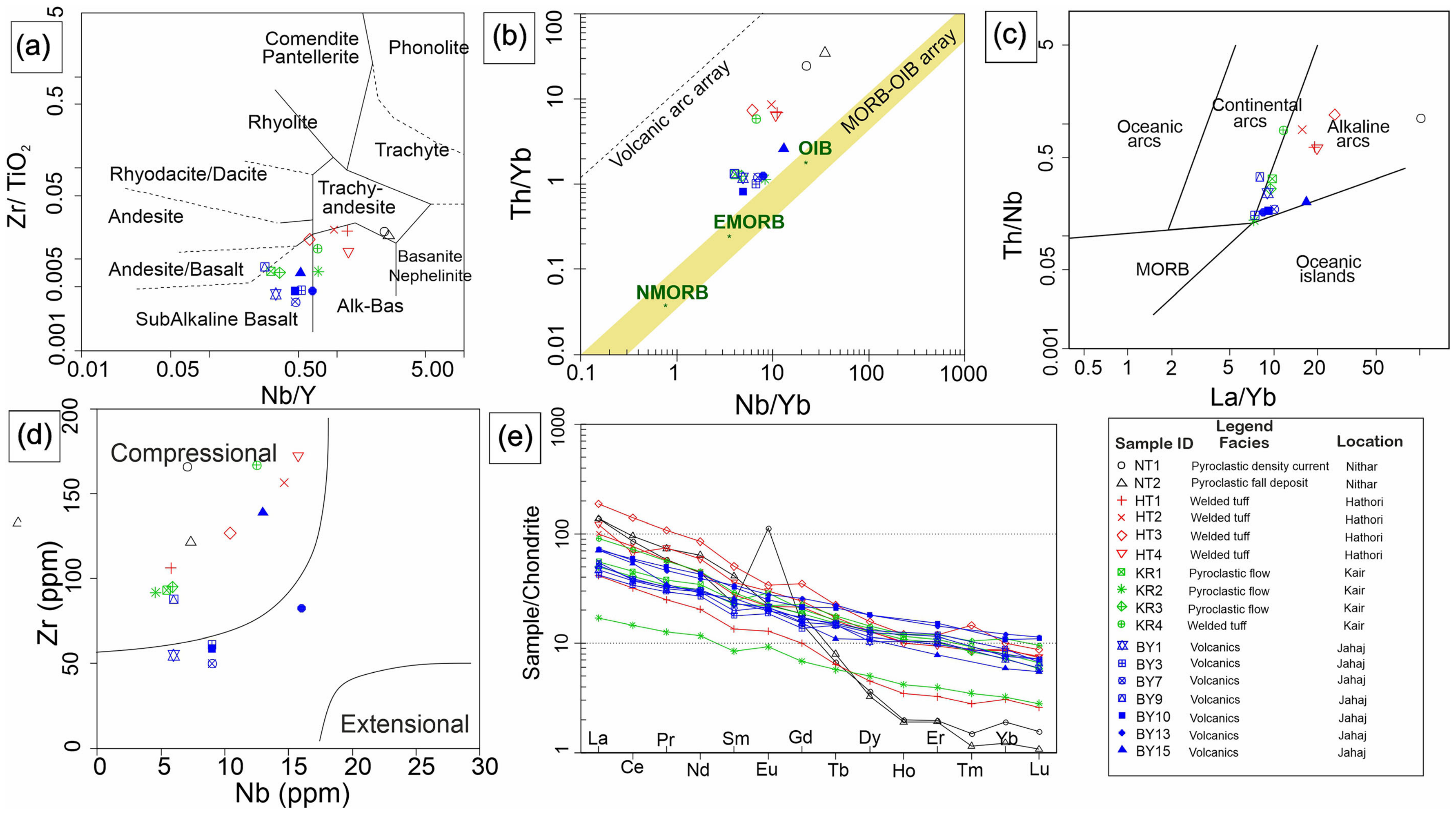

Figure 11. In Nb/Y *vs.* Zr/TiO$_2$ plot (after Winchester and Floyd 1977) pyroclastic lava flow samples (KR1–3) plot in a subalkaline basalt field whereas welded tuff samples (HT1–4) dominantly fall along the boundary between alkali basalt and trachy-andesite (**a**); In Nb/Yb *vs.* Th/Yb plot (after Pearce 2008) (**b**), and La/Yb *vs.* Nb/La plot (**c**), volcaniclastic samples fall in the fields of continental arcs, alkaline arcs, and marginally in the oceanic islands field; Zr/Nb plot of Bayana volcaniclastics (**d**) showing dominant compressional tectonic set up; (**e**) and chemical plot of rare earth elements of volcaniclastics normalized against chondrite (Sun and McDonough 1989) (**e**).

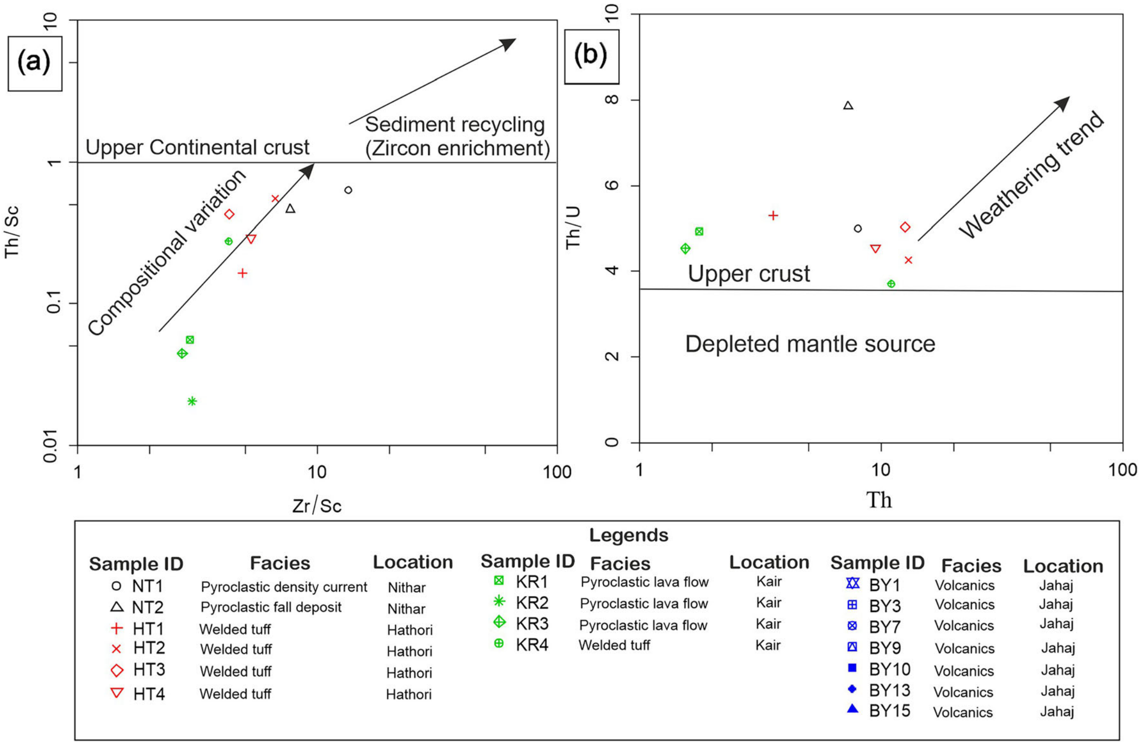

Figure 12. Discrimination diagrams illustrating weathering and sediment recycling: (**a**) Th/Sc and Zr/Sc diagram illustrating volcaniclastics of the Bayana sub-basin largely representative of the composition of parent magmatic source and without much influence of sediment recycling and (**b**) Th/U *vs.* Th plot indicating first cycle volcanogenic sediment.

Th/Sc value of <0.1 indicate mafic composition. In addition, a plot involving Th/Sc and Zr/Sc allowed us to infer that the geochemical composition of Bayana volcaniclastics is largely representative of the composition of the parent magmatic source without much influence from sedimentary processes (figure 12a; cf. McLennan *et al.* 1993; Xiang *et al.* 2015).

Corroboration in favour of the contention comes from the Th/U ratio in volcaniclastics, which provides a clue in understanding the degree of weathering and recycling due to loss and oxidation of uranium (McLennan *et al.* 1990, 1993; Xiang *et al.* 2015). The values of Th/U ratio of the volcaniclastic units vary from 3.71 to 5.30 (average 4.67) with one sample from unit NT-2 having a ratio of 7.85, which are higher than that of UCC (3.8; Taylor and McLennan 1985) (figure 11b). The lack of well-defined correlation of Th/U with Al_2O_3 in volcaniclastic samples construes that the volcaniclastics, in general, are derived from source magmatic clan with a low degree of weathering and with sparse recycled sediment (Meinhold *et al.* 2007). The higher Th/U ratio in NT2 may be due to the higher concentration of Th over U (0.63–12.95 ppm and 0.13–3.05 ppm, respectively) compared to UCC (10.07 and 2.8 ppm, respectively; Taylor and McLennan 1985) and is attributed to the solubility of oxidized uranium in comparison to rather immobile Th.

The Th concentration and Th *vs.* Nb ratio of Pearce (2008) (i.e., Th/Yb *vs.* Nb/Yb) are chosen to throw light on the crustal contamination component. Except for pyroclastic flow samples (KR1–3), volcaniclastic samples unequivocally record high Th concentration (average 9.24 ppm; $n = 7$). In Th/Yb *vs.* Nb/Yb plot (figure 11b), present-day MORB and OIB form a diagonal array with average N-MORB, E-MORB, and OIB at its center. All magmatic-origin samples (volcanic rocks and volcaniclastics) from Bayana are displaced to higher Th/Yb values and thereby plot above the array. This may indicate (i) increasing differentiation of the magma or (ii) interaction of ascending magma with continental crust, or (iii) an ancient subduction component, as suggested by Cow and Condie (1988).

Chondrite-normalized REE plot (after Sun and McDonough 1989) from the volcanic rocks and volcaniclastics reveals a LREE enriched and nearly flat HREE pattern (figure 11e). Only pyroclastic massflow and fall samples from the Nithar section (NT1 and 2) display extremely low HREE distribution. The average $(La/Yb)_N$ value for Nithar village samples (pyroclastic conglomerate and fall) is 92.23, whereas that of the Hathori village samples (welded tuff, HT1–4, and KR4) is 13.24, that of Kair village samples (pyroclastic flow, KR1–3) is 6.35, and that of volcanic rocks samples (BY1–BY15) is 7.06. Though most of the samples do not display any significant Europium (Eu) anomaly (marginally negative to marginally positive), only the sample NT1 (pyroclastic conglomerate) records a strong positive Eu anomaly. In general, $Eu/Eu^* = Eu/(Sm^*Gd)^{0.5}$ values of the volcaniclastics in this study vary between 0.8 and 1.27 with an average of 1.02 (except 6.1 for NT1 sample). This suggests an accumulation of plagioclase feldspar in the melt, a trend that is most pronouncedly visible in the sample NT1. The depletion of HREE in NT1 and NT2 bears an indication of crystallization of zircon from the melt (Winter 2013).

6. Discussion

From the presence of volcanic and volcaniclastics rocks present at multiple stratigraphic levels of Jahaj–Govindpura Formation within the Raialo Group litho-succession, it is suggested that the Bayana basin was thermally active during its early riftogenic sedimentation history. On an extending and subsiding cratonic basement, rapid sedimentation and high burial rate might have prevented deep-rooted weathering of coarse-grained volcaniclastics and hence, allowed their preservation and present documentation. The presence of subangular, block/bomb clasts within pyroclastic conglomerates (VLC 3) bears an undoubted indication of short transport distance, possibly from the graben flank to the valley. In a west–east transect (figure 2), (i) a change in the grain size of volcanic clast from coarse to fine-grained, (ii) a change in associated sedimentary facies type from continental to shallow marine, and (iii) an unequivocal eastward paleocurrent pattern, all point towards a proximal-distal relationship with subaerial to subaqueous transition from the west (Nithar section) to east (Kair section). At the western-most Nithar section, volcaniclastic beds of facies type VLC 3 (bouldery volcaniclastics as pyroclastic density current/pyroclastic debris (mass) flows) and VLC 4 (pyroclastic fall) are recorded in association with poorly-sorted trough cross-stratified alluvial sediments having unimodal northeastward paleocurrent pattern. Eastward at the Hathori section, interbedded pyroclastic fall (VLC 4)/ rare thin-bedded finer-grained counterparts of VLC 3 and poorly-sorted alluvial sediment (unimodal northeastward paleocurrent), give way upward to beds and laminations of welded tuff (VLC 2) interlayered with siltstone-shale succession preserve wave evidence such as wave ripple, hummocky cross stratification and bimodal paleocurrent pattern. Based on these observations, an upward transition from subaerial to the subaqueous condition of volcaniclastic emplacement is inferred from the Hathori section. In the easternmost Kair section pyroclastic lava flow (VLC 1) and counterparts of welded tuff units (VLC 2) are noticed in alternation with medium-grained ripple-laminated sandstone with bimodal paleocurrent at the basal part and with the thinly-bedded siltstone-shale unit in the upper part. A shallow to deep-water subaqueous emplacement of pyroclastics is inferred at the Kair section. A generalized paleogeographic illustration of the Jahaj–Govindpura Formation depositional setting with emphasis on sedimentary and volcaniclastic facies variants is presented in figure 13. From sediment petrography and general paleocurrent analysis, Ahmad *et al.* (2012) identified Archean Craton including Dausa uplift, present in the west and south of the basin, as possible sediment provenance for the basin. Supporting the idea, the northeastward paleocurrent obtained under present study points towards volcaniclastic supply from eruptive activities in the west–southwest, in the footwall of the graben.

En-masse freezing (Wright and Walker 1981; Carey 1991) and progressive aggradation (Branney and Kokelaar 1992) are two accepted models for PDC deposition. Whereas massive PDCs with lobate front suggest abrupt halt and en-masse freezing of the flow triggered by internal yield strength (Sparks 1976; Miyabuchi 1999), the amalgamated graded pyroclastic flow beds without much change in bed thickness suggest progressive aggradation with a continuous supply of material in the boundary shear zone of the flow. High clast concentration in the basal part of several PDC beds exposed at the Nithar section is the result of relative segregation and settlement of particles of higher settling velocity in stratified flow (Dellino *et al.* 2004; Sulpizo *et al.* 2014). The intervention of pyroclastic fall (VLC 4) deposit in between variably thick conglomeratic units bears indication of stepwise deposition of PDCs with periods of a steady or sharp increase in the deposit thickness and periods of suspension deposition. A progressive

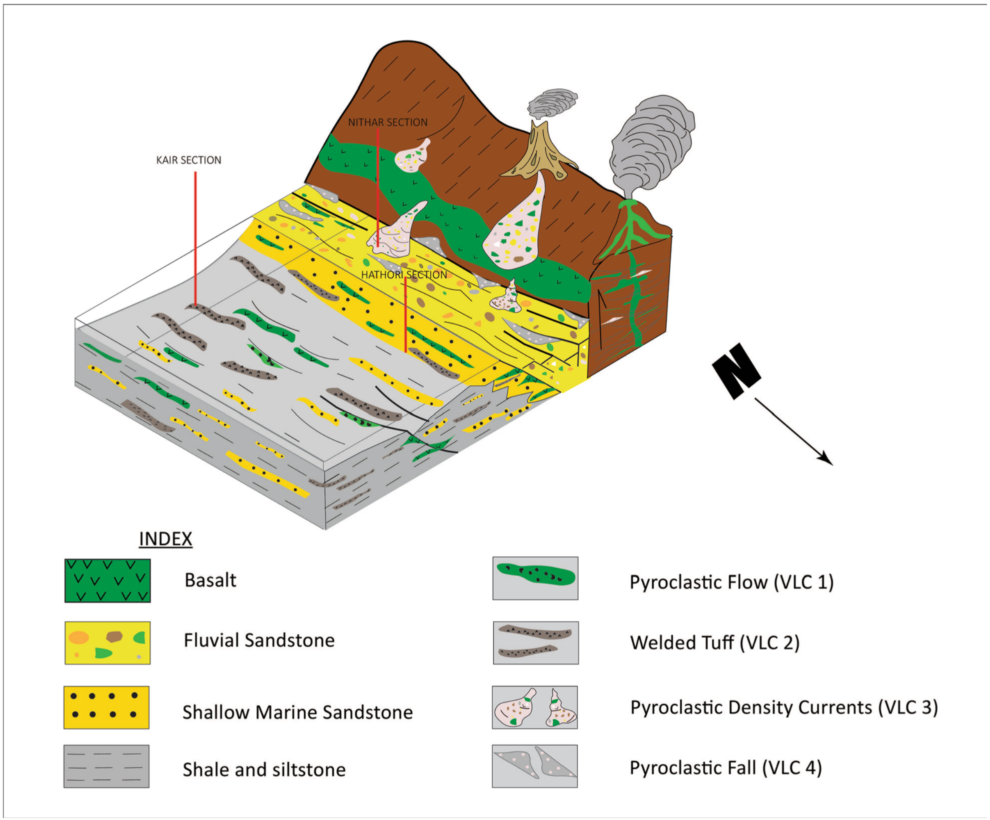

Figure 13. A cartoon (not to scale) illustrating the depositional model for volcaniclastics and volcanic rocks from the Raialo Group of the Bayana sub-basin, NDFB emphasizing sedimentary environments of a half-graben related setting.

aggradation model is visualized for the pyroclastic flow deposit exposed at the Kair section since the amalgamated units do not show any major change in layer thickness or composition.

Absence of any significant overprinting because of metamorphism, deformation or burial compaction allowed preservation of original textures in the volcaniclastic rocks. The petrographic evidence including clast annealing, deformation in fine pumice fragments, eutaxitic foliation, and shattered crystals (cf. Fisher 1984), corroborates the subaquatic emplacement model for volcaniclastics present at the upper part of Hathori and Kair sections, as inferred from nature of associated sedimentary facies. Additionally, different shapes of glass shards viz. curved, cuspate, elongate (c.f., Fisher and Schmincke 1984), well-sorted grain size (Cashman and Fiske 1991), evidence of welding and strong alteration of glass into zeolite, further strengthen the subaquatic emplacement model (Heiken 1972; Heiken and Wohletz 1985). In contrast, associated with terrestrial alluvial deposits, the PDCs at the Nithar section, with variable particle concentration and well-stratified character, resemble flows in which particle segregation led to the development of a bipartite character with a high-concentration flow phase (affected by particle interaction and pore-fluid pressure) that is overlain by dilute low-concentration turbulent phase (dominated by fluid drag). Ash clouds emanating from PDCs can be substantial (Major 2022) and produce fall deposits, as seen at the Nithar section (VLC 4) in alternation with PDCs. Though there is a possibility of reworking subaerial volcaniclastics and their subsequent emplacement in subaquatic conditions (secondary deposition), in the absence of any tell-tale feature indicating secondary emplacement, the present study considers both subaerial and subaqueous deposits in the study area as primary deposits directly from the eruption.

On collation of available geochemical data from volcanic and volcaniclastic rocks under the present study, we made several observations (i) volcanic rocks with low SiO_2, K_2O, and TiO_2, and high Mg number fall in the basaltic field, whereas volcaniclastics with higher and variable SiO_2 contents, high K_2O, Al_2O_3, TiO_2, and low Mg number define a wide range of composition varying between trachybasalt, trachyandesite, basaltic andesite, and rhyolite (figure 10b), (ii) volcaniclastics, in general, record high Ba values; samples from bouldery pyroclastic mass flow conglomerate record very high value, (iii) despite high Cr contents in all variants of volcaniclastics, high Sr and Rb contents are recorded in the pyroclastic flow and welded tuff samples, respectively, (iv) except for pyroclastic flow, volcaniclastics, in general, yield high Zr contents, and (v) an enrichment of LIL elements and Th within the volcaniclastics with an average Th/Sc ratio of 0.42. The major element compositions give a general impression in favour of tholeiitic basalt, calc-alkaline to rhyolite composition for the source magma clan. Possibly volcanic source rocks were more basic (low SiO_2, high MgO) and tholeiitic to calc-alkaline island arc source composition compared to volcaniclastics, which had a more intermediate to felsic in composition. From observations including enrichment of LIL elements, high Th, Sr, Rb, Zr, and Th/Sc values, it is inferred that the Bayana volcaniclastics record the geochemical signature of magma differentiation and/or crustal contamination either as a result of interaction between ascending magma and continental crust or by sediment entrainment in course of transportation history. An overall subduction-related setting (continental to alkaline) is inferred from Th/Yb *vs.* Nb/Yb plots (figure 11b), Th/Nb *vs.* La/Yb (figure 11c), and Zr *vs.* Nb (figure 11d). The high Ba content within the volcaniclastics is traced in the presence of Ba–K bearing feldspar Celsian in the system. In this setting, it is argued that the Bayana rift basin initiated in a plate margin under an overall subduction-related tectonic set-up, not as an intracratonic rift as surmised in earlier studies (Singh 1982, 1985, 1988). Interestingly, Naik *et al.* (2022), in a recent study, also contemplated a subduction-related setting for the NDFB from new age data and a high-pressure clock-wise (prograde) segment of the P–T–t path reconstructed from the metamorphic assemblage of the Alwar and Khetri sub-basins. Citing the absence of any pre-Delhi aged rocks on the west of the Delhi Fold Belt (DFB including both NDFB and SDFB) these authors argued against an intracratonic set-up for the NDFB basins.

6.1 *Regional to the global tectonic implication*

The supercontinent Columbia was stitched together by many internal orogenic belts within the timeframe of ca. 2000–1700 Ma (Zhao *et al.* 2002), the peak of such orogenesis falls in the ca. 1900–1850 Ma time bracket (Rogers and Santosh 2009), which bear indication for the amalgamation of the supercontinent in the time. A late Paleoproterozoic age of 1876 Ma (Deb and Thorpe 2004) obtained from the Bayana rhyodacite tuff coincides well with timeframe of the assembly of the Columbia supercontinent (Zhao *et al.* 2003; Hou *et al.* 2008; Zhang *et al.* 2012; Kusky *et al.* 2016).

Geochemically, the basaltic to calc-alkaline volcanic rocks and volcaniclastics within the Raialo Group of rocks in the presently-studied Bayana succession bear signature of a subduction margin in the near vicinity of the eastern NDFB. Bhowmik and Dasgupta (2012) envisaged a west-ward subduction (with respect to the present-day disposition of lithounits in the Aravalli–Delhi mobile belt) of oceanic plate that was formed between the rifted preexisting Archean Banded Gneissic complex of the Aravalli Craton. This island arc/continental arc collision coeval with subduction matches agewise with the amalgamation of Columbia. Further, the rock record of the orogenesis, i.e., the tectonothermal and magmatic events during this time lies in the deep crustal metasedimentary rocks of the Sandmata Metamorphic Complex and Mangalwar Metamorphic Complex (Buick *et al.* 2006, 2010), calc-alkaline plutonic rocks in the North Delhi Fold Belt (Kaur *et al.* 2009), the Anasagar granite gneiss rocks (Mukhopadhyay *et al.* 2023). Description of similar subduction-related orogenic processes related to the amalgamation of Columbia are though rare but reported from other parts of the Indian continent, e.g., southern Eastern Ghats Belt (Kumar *et al.* 2010; Bose *et al.* 2011) Similar ages are also reported as the age of deep crustal tectonothermal events from the high-pressure granulites and eclogites (Tsunogae *et al.* 2011; Zhai and Santosh 2011) and considered as a signature of the Trans-North China Orogen (TNCO) that eventually form the present tectonic framework of the North China Craton (NCC; Zhao and Zhai 2013; Kimura *et al.* 2021). This significant tectonic movement that occurred in the late Paleoproterozoic is also referred to as the Lüliang Movement in the North China Craton (Wang and Mo 1995). Altogether, the Paleoproterozoic cratonic China, one of the erstwhile neighbours of the Indian Craton in the Columbia architecture (Zhang *et al.* 2012) bear the signature of a crustal-scale collisional event (Bhowmik and Dasgupta 2012; Kusky *et al.* 2016). Interestingly, several basins in the amalgamated Columbia formed during the end of such orogens at ca. 1800 Ma, i.e., Aravalli Orogen in India and TNCO in China. In the North China Craton, rift basins were successively formed from south to north, namely, Xiong'er Basin at the southern margin to Yanliao Basin at the northern margin (Zhai *et al.* 2015; Deng *et al.* 2021). The earliest history of such basins can be traced in the Xiong'er Group of the Xiong'er Basin. An early stage of the basin-fill in the riftogenic Xiong'er Basin is dominated by mafic volcanic rocks and volcaniclastic rocks. The present documentation of volcaniclastics of calc-alkaline affinity in the Bayana Basin, in terms of the tectonic setting and timing, shares a common history of volcanism and coeval sedimentary basin formation with the other parts of the pre-existing cratonic blocks (e.g., North China Craton) and hence, strengthens the Columbia architecture, as proposed by Zhang *et al.* (2012). With a surge of high-resolution data from continental China in recent years, we restrict our search for similar tectonic histories only to Paleoproterozoic India and China. However, we also believe that similar shallow crustal products in response to such transcontinental-scale rearrangement of crustal blocks during their amalgamation process can be traced in the presently dismembered continents for the sake of a better understanding of coupled interaction between mantle-deep crust-shallow crust-ocean-atmosphere during the history of a supercontinent.

7. Conclusions

(1) Volcaniclastics with varied lithology and rheology are documented from different stratigraphic levels of the Raialo Group, exposed in the Bayana sub-basin of NDFB. From a detailed facies analysis four different characters and rheology viz. pyroclastic flow welded tuff, clast-/matrix-supported boulder pyroclastic conglomerate, and pyroclastic fall deposits (VLC 1–4) are documented.

(2) In a west–east transect, taking into consideration the characters of associated sedimentary facies types and paleocurrent pattern, a proximal-distal relationship between different volcaniclastic facies variants was established in subaerial to subaqueous settings; whereas pyroclastic lava flow and welded tuff are identified as subaqueous deposits, clast-/matrix-supported boulder pyroclastic conglomerate, and pyroclastic fall are kept under the subaerial category.

(3) An attempt is made to collate available geochemical data from the Jahaj–Govindpura volcanic rocks and new geochemical (major, trace element, and REE) data generated from volcaniclastics in the present study. Volcanic rocks with low SiO_2 and high MgO resemble tholeiitic to calc-alkaline island arc composition, whereas a more intermediate to felsic composition is inferred for the volcaniclastics. An enrichment of LIL elements, i.e., Th, Sr, Rb, Zr, and Th/Sc values within Bayana volcaniclastics suggests magma differentiation and/or crustal contamination either as a result of interaction between ascending magma and continental crust or by sediment entrainment in the course of transportation history.

(4) Opening of the Bayana rift basin in an overall subduction-related setting is argued from trace element and REE geochemistry of volcaniclastics, instead of an intracratonic model proposed in earlier studies.

(5) In terms of tectonic setting and depositional timing, the Bayana volcanic and volcaniclastic rocks share a common depositional history with contemporary basins within North China craton and thereby strengthen the supercontinent Columbia architecture.

Acknowledgements

PPC acknowledges the financial help from Institute of Eminence (IOE), University of Delhi in terms of Faculty Recharge Programme (FRP). RB acknowledges financial help from the Council of Industrial Research (CSIR) in terms of fellowship. Infrastructural help from Department of Geology, University of Delhi, thankfully acknowledged.

Author statement

SBR, PPC and RB carried out field work and conceptualized the problem. NML and KD were involved in analytical data generation. SBR, PPC, RB, KD and SS participated in the manuscript write-up, conceptualization of figures and data interpretation.

References

Ahmad A H M, Saikia C and Wasim S M 2012 Petrofacies evolution of Bayana Basin sandstones of Mesoproterozoic Delhi Supergroup, Bharatpur District, Rajasthan, North-western India; *Open J. Geol.* **2(04)** 260.

Alam M M and Ahmad A H M 2000 Lithofacies and Petrofacies analysis of alluvial fan deposits of the Bayana formation, Bharatpur district, Rajasthan; *Indian Miner.* **54** 233–244.

Alam M M, Mondal M E A and Ahmad A H M 2006 Tectonic significance of syn-sedimentary volcanism: Evidence from sandstone Detritus, Bayana Basin, Delhi supergroup; *J. Geol. Soc. India* **68** 648.

Altermann W and Lenhardt N 2012 The volcano-sedimentary succession of the Archean Sodium Group, Ventersdorp Supergroup, South Africa: Volcanology, sedimentology and geochemistry; *Precamb. Res.* **214** 60–81.

Bagnold R A 1954 Experiments on a gravity-free dispersion of large solid spheres in a Newtonian fluid under shear; *Proc. R. Soc. London, Ser. A: Math. Phys. Sci.* **225** 49–63.

Banerjee A K and Singh S P 1977 Sedimentary tectonics of Bayana sub-basin of northeastern Rajasthan; *J. Indian Assoc. Sedimentol.* **1** 74–85.

Barkat R, Chakraborty P P, Saha S and Das K 2020 Alluvial architecture, paleohydrology and provenance tracking from the Neoproterozoic Banganapalle formation, Kurnool Group, India: An example of continental sedimentation before land plants; *Precamb. Res.* **350** 105930, https://doi.org/10.1016/j.precamres.2020.105930.

Bergh S G and Torske T 1988 Palaeovolcanology and tectonic setting of a Proterozoic metatholeiitic sequence near the Baltic Shield margin, northern Norway; *Precamb. Res.* **39** 227–246.

Bhowmik S K and Dasgupta S 2012 Tectonothermal evolution of the Banded Gneissic Complex in central Rajasthan, NW India: Present status and correlation; *J. Asian Earth Sci.* **49** 339–348.

Bose S, Dunkley D J, Dasgupta S, Das K and Arima M 2011 India–Antarctica–Australia–Laurentia connection in the Paleoproterozoic-Mesoproterozoic revisited: Evidence from new zircon U–Pb and monazite chemical age data from the Eastern Ghats Belt, India; *Geol. Soc. Am. Bull.* **123** 2031–2049, https://doi.org/10.1130/B30336.1.

Branney M J and Kokelaar P 1992 A reappraisal of ignimbrite emplacement: Progressive aggradation and changes from particulate to non-particulate flow during emplacement of high-grade ignimbrite; *Bull. Volcanol.* **546(54)** 504–520, https://doi.org/10.1007/BF00301396.

Branney M J and Kokelaar B P 2002 Pyroclastic density currents and the sedimentation of ignimbrites; *Geol. Soc. London.*

Brown R J and Branney M J 2013 Internal flow variations and diachronous sedimentation within extensive, sustained, density-stratified pyroclastic density currents flowing down gentle slopes, as revealed by the internal architectures of ignimbrites on Tenerife; *Bull. Volcanol.* **75** 1–24.

Buick I S, Allen C, Pandit M, Rubatto D and Hermann J 2006 The Proterozoic magmatic and metamorphic history of the Banded Gneiss Complex, central Rajasthan, India: LA-ICP-MS U-Pb zircon constraints; *Precamb. Res.* **151** 119–142.

Buick I S, Clark C, Rubatto D, Hermann J, Pandit M and Hand M 2010 Constraints on the Proterozoic evolution of the Aravalli-Delhi Orogenic belt (NW India) from monazite geochronology and mineral trace element geochemistry; *Lithos* **120** 511–528.

Bull K F and McPhie J 2007 Fiamme textures in volcanic successions: Flaming issues of definition and interpretation; *J. Volcanol. Geotherm. Res.* **164** 205–216.

Calder E S, Cole P D, Dade W B, Druitt T H, Hoblitt R P, Huppert H E, Ritchie L, Sparks R S J and Young S R 1999 Mobility of pyroclastic flows and surges at the Soufriere Hills Volcano, Montserrat; *Geophys. Res. Lett.* **26** 537–540.

Carey S N 1991 Transport and deposition of tephra by pyroclastic flows and surges; *Sedimentation in Volcanic Settings* **45** 39–57.

Cas R A F and Wright J V 1987 *Volcanic successions: Ancient and modern*; Allen and Unin, London.

Cas R and Busby-Spera C 1991 *Volcaniclastic sedimentation*; Elsevier.

Cashman K V and Fiske R S 1991 Fallout of pyroclastic debris from submarine volcanic eruptions; *Science* **253(5017)** 275–280.

Chambers F M, Daniell J R G, Hunt J B, Molloy K and O'Connell M 2004 Tephrostratigraphy of An Loch Mor, Inis Oirr, western Ireland: Implications for Holocene tephrochronology in the northeastern Atlantic region; *Holocene* **14(5)** 703–720.

Chang Q, Shibata T, Shinotsuka K, Yoshikawa M and Tatsumi Y 2003 Precise determination of trace elements in geological standard rocks using inductively coupled plasma mass spectrometry (ICP-MS); *Front. Res. Earth Evol.* **1** 357–362.

Chang Y, Li J and Song C 2019 The regional tectonic framework and some new understandings of the Middle-Lower Yangtze River Valley Metallogenic Belt; *Acta Petrol. Sin.* **35** 3579–3591.

Charbonnier S J and Gertisser R 2011 Deposit architecture and dynamics of the 2006 block-and-ash flows of Merapi Volcano, Java, Indonesia; *Sedimentology* **58** 1573–1612.

Condie K C 1993 Chemical composition and evolution of the upper continental crust: Contrasting results from surface samples and shales; *Chem. Geol.* **104** 1–37.

Cousineau P A 1994 Subaqueous pyroclastic deposits in an Ordovician fore-arc basin: An example from the Saint-Victor Formation, Quebec Appalachians, Canada; *J. Sediment. Res.* **64** 867–880.

Crow C and Condie K C 1987 Geochemistry and origin of late Archean volcanic rocks from the Rhenosterhoek Formation, Dominion Group, South Africa; *Precamb. Res.* **37** 217–229.

Cullers R L, Basu A and Suttner L J 1988 Geochemical signature of provenance in sand-size material in soils and stream sediments near the Tobacco Root batholith, Montana, USA; *Chem. Geol.* **70** 335–348.

Cullers R L 2000 The geochemistry of shales, siltstones and sandstones of Pennsylvanian-Permian age, Colorado, USA: Implications for provenance and metamorphic studies; *Lithos* **51(3)** 181–203, https://doi.org/10.1016/S0024-4937(99)00063-8.

De Schutter A, Kervyn M, Canters F, Bosshard-Stadlin S A, Songo M A and Mattsson H B 2015 Ash fall impact on vegetation: A remote sensing approach of the Oldoinyo Lengai 2007–08 eruption; *J. Appl. Volcanol.* **4** 1–18.

Deb M and Thorpe R I 2004 Geochronological constraints in the Precambrian geology of Rajasthan and their metallogenic implications; Sediment-hosted lead-zinc sulphide deposits; Narosa publication house, New Delhi, pp. 246–263.

Dellino P, Isaia R and Veneruso M 2004 Turbulent boundary layer shear flows as an approximation of base surges at Campi Flegrei (Southern Italy); *J. Volcanol. Geotherm. Res.* **133** 211–228.

Dellino P, Büttner R, Dioguardi F, Doronzo D M, La Volpe L, Mele D, Sonder I, Sulpizio R and Zimanowski B 2010 Experimental evidence links volcanic particle characteristics to pyroclastic flow hazard; *Earth Planet. Sci. Lett.* **295** 314–320.

Deng Y, Wang H, Lyu D, Zhang F, Gao Z, Ren R, Ye Y, Lyu Y, Wang X and Guan P 2021 Evolution of the 1.8–1.6 Ga Yanliao and Xiong'er basins, north China Craton; *Precamb. Res.* **365** 106383.

Denlinger R P and Iverson R M 2001 Flow of variably fluidized granular masses across three-dimensional terrain 2. Numerical predictions and experimental tests; *J. Geophys. Res. Solid Earth* **106** 553–566, https://doi.org/10.1029/2000jb900330.

DeWolfe Y M and Pittman N 2018 Subaqueous strombolian eruptions, and eruption-fed pyroclastic deposits in a Paleoproterozoic rifted-arc: Hidden formation, Flin Flon, Canada; *Precamb. Res.* **316** 48–65.

Druitt T H 1998 Pyroclastic density currents; *Geol. Soc. Spec. Publ.* **145** 145–182, https://doi.org/10.1144/GSL.SP.1996.145.01.08.

Fisher R V 1961 Proposed classification of volcaniclastic sediments and rocks; *Geol. Soc. Am. Bull.* **72** 1409–1414.

Fisher R V 1966 Rocks composed of volcanic fragments and their classification; *Earth Sci. Rev.* **1** 287–298, https://doi.org/10.1016/0012-8252(66)90010-9.

Fisher R V 1979 Models for pyroclastic surges and pyroclastic flows; *J. Volcanol. Geotherm. Res.* **6** 305–318.

Fisher R V 1984 Submarine volcaniclastic rocks; *Geol. Soc. London Spec. Publ.* **16** 5–27.

Fisher R V and Schmincke H U 1984 Alteration of volcanic glass, In: *Pyroclastic Rocks*; Springer, pp. 312–345.

Fisher R V and Smith G A 1991 Volcanism, tectonics and sedimentation.

Freundt A, Hartmann A, Kutterolf S and Strauch W 2010 Volcaniclastic stratigraphy of the Tiscapa maar crater walls (Managua, Nicaragua): Implications for volcanic and seismic hazards and Holocene climate changes; *Int. J. Earth Sci.* **99** 1453–1470.

Garzanti E 1986 Source rock versus sedimentary control on the mineralogy of deltaic volcanic arenites (Upper Triassic, northern Italy); *J. Sediment. Petrol.* **56(2)** 267–275.

Gawthorpe R L and Leeder M R 2000 Tectono-sedimentary evolution of active extensional basins; *Basin Res.* **12** 195–218, https://doi.org/10.1111/j.1365-2117.2000.00121.x.

Gibson H L, Morton R L and Hudak G J 1997 Submarine volcanic processes, deposits, and environments favorable for the location of volcanic-associated massive sulfide deposits, https://doi.org/10.5382/Rev.08.02.

Gifkins C C, Allen R L and McPhie J 2005 Apparent welding textures in altered pumice-rich rocks; *J. Volcanol. Geotherm. Res.* **142(1–2)** 29–47.

Gloppen T G and Steel R J 1981 The deposits, internal structure and geometry in six alluvial fan-fan delta bodies (Devonian-Norway) – A study in the significance of bedding sequence in conglomerates; *J. Sediment. Res.* **53** 325–329, https://doi.org/10.1306/212F81CA-2B24-11D7-8648000102C1865D.

Goswami S, Upadhyay P K, Bhagat S, Zakaulla S, Bhatt A K, Natarajan V and Dey S 2018 An approach of understanding acid volcanic and tuffaceous volcaniclastics from field studies: A case from Tadpatri Formation, Proterozoic Cuddapah basin, Andhra Pradesh, India; *J. Earth Syst. Sci.* **127** 1–21.

Goswami S, Dey S, Zakaulla S and Verma M B 2020 Active rifting and bimodal volcanism in Proterozoic Papaghni subbasin, Cuddapah basin (Andhra Pradesh), India; *J. Earth Syst. Sci.* **129** 1–31.

Grunder A and Russell J K 2005 Welding processes in volcanology: Insights from field, experimental, and modeling studies; *J. Volcanol. Geotherm. Res.* **142** 1–9.

Grunder A L, Laporte D and Druitt T H 2005 Experimental and textural investigation of welding: Effects of compaction, sintering, and vapor-phase crystallization in the rhyolitic Rattlesnake Tuff; *J. Volcanol. Geotherm. Res.* **142** 89–104.

Gupta S, Cowie P A, Dawers N H and Underhill J R 1998 A mechanism to explain rift-basin subsidence and stratigraphic patterns through fault-array evolution; *Geology* **26** 595–598.

Hampton M A 1972 The role of subaqueous debris flow in generating turbidity currents; *J. Sediment. Res.* **42**.

Hao P, Cheng Y I N, Qinglin H E, Guoyong X I A, Yong L I U, Tinghu M A, Kang C, Ran L I U and Wang S U 2022 Development characteristics and petroleum geological significance of Permian pyroclastic flow volcanic rocks in Western Sichuan Basin, SW China; *Pet. Explor. Dev.* **49** 64–77.

Hasnat Masood Ahmad A, Saikia C and Mohammad Wasim S 2012 Petrofacies evolution of Bayana Basin Sandstones of Mesoproterozoic Delhi Supergroup, Bharatpur district, Rajasthan, Northwestern India; *Open J. Geol.* **02** 260–270, https://doi.org/10.4236/ojg.2012.24026.

Heiken G 1972 Morphology and petrography of volcanic ashes; *Geol. Soc. Am. Bull.* **83** 1961–1988.

Heiken G and Wohletz K 1985 *Volcanic ash*; University Presses of California, Chicago, Harvard & MIT.

Hiscott R N and Gill J B 1992 Major and trace element geochemistry of Oligocene to Quaternary volcaniclastic sands and sandstones from the Izu–Bonin Arc; In: *Proceedings of the Ocean Drilling Program, Scientific Results*, Government Printing Office College Station Texas, pp. 467–486.

Hinchey A M 2021 Lithofacies architecture and paleoenvironment of a Paleoproterozoic volcano-sedimentary sequence: Insight into rift-related volcanism during supercontinent assembly; *Precamb. Res.* **367** 106443.

Hou G, Santosh M, Qian X, Lister G S and Li J 2008 Configuration of the Late Paleoproterozoic supercontinent Columbia: Insights from radiating mafic dyke swarms; *Gondwana Res.* **14** 395–409, https://doi.org/10.1016/j.gr.2008.01.010

Houghton B and Carey R J 2015 Pyroclastic fall deposits, In: *The Encyclopedia of Volcanoes*, Elsevier, pp. 599–616.

Jensen L S 1976 A new plot for classifying subalkalic volcanic rocks; *Ontario Div. Mines, Misc.* **66** 1–22.

Kaur P, Chaudhri N, Raczek I, Kröner A and Hofmann A W 2009 Record of 1.82 Ga Andean-type continental arc magmatism in NE Rajasthan, India: Insights from zircon and Sm–Nd ages, combined with Nd–Sr isotope geochemistry; *Gondwana Res.* **16** 56–71.

Kimura K, Hayasaka Y, Yamashita J, Shibata T, Kawaguchi K, Fujiwara H and Das K 2021 Antiquity and tectonic lineage of Japanese Islands: New discovery of Archean-Paleoproterozoic Complex; *Earth Planet. Sci. Lett.* **565** 116926, https://doi.org/10.1016/J.EPSL.2021.116926.

Kokelaar P and Busby C 1992 Subaqueous explosive eruption and welding of pyroclastic deposits; *Science* **257(5067)** 196–201.

Köykkä J 2011 Precambrian alluvial fan and braidplain sedimentation patterns: Example from the Mesoproterozoic Rjukan Rift Basin, southern Norway; *Sediment. Geol.* **234** 89–108, https://doi.org/10.1016/j.sedgeo.2010.12.004.

Kumar K V, Ernst W G, Leelanandam C, Wooden J L and Grove M J 2010 First Paleoproterozoic ophiolite from Gondwana: Geochronologic–geochemical documentation of ancient oceanic crust from Kandra, SE India; *Tectonophysics* **487** 22–32.

Kusky T M, Polat A, Windley B F, Burke K C, Dewey J F, Kidd W S F, Maruyama S, Wang J P, Deng H and Wang Z S 2016 Insights into the tectonic evolution of the North China Craton through comparative tectonic analysis: A record of outward growth of Precambrian continents; *Earth-Sci. Rev.* **162** 387–432.

Lambiase J J and Bosworth W 1995 Structural controls on sedimentation in continental rifts; *Geol. Soc. London Spec. Publ.* **80** 117–144.

Le Bas M, Maitre R L, Streckeisen A, Zanettin B and IUGS Subcommission on the Systematics of Igneous Rocks 1986 A chemical classification of volcanic rocks based on the total alkali-silica diagram; *J. Petrol.* **27(3)** 745–750.

Lenhardt N, Masango S M, Jolayemi O O, Lenhardt S Z, Peeters G J and Eriksson P G 2017 The Palaeoproterozoic (∼2.06 Ga) Rooiberg Group, South Africa: Dominated by extremely high-grade lava-like and rheomorphic ignimbrites? New observations and lithofacies analysis; *J. Asian Earth Sci.* **131** 213–232.

Lenhardt N, Bleeker W, Ngwa C N and Aucamp T 2020 Shallow marine basaltic volcanism of the Machadodorp Member (Silverton Formation, Pretoria Group), Transvaal Basin, South Africa – An example of Paleoproterozoic explosive intraplate volcanic activity in an epeiric embayment; *Precamb. Res.* **338** 105580.

Le Roux J P 2003 Can dispersive pressure cause inverse grading in grain flows?: Discussion; *J. Sediment. Res.* **73** 333–334.

Lucas-Tooth J and Pyne C 1963 The accurate determination of major constituents by X-ray fluorescent analysis in the presence of large interelement effects; *Adv. X-Ray Anal.* **7** 523–541.

Mahood G A 1984 Pyroclastic rocks and calderas associated with strongly peralkaline magmatism; *J. Geophys. Res. Solid Earth* **89** 8540–8552.

Major J J 2022 Subaerial volcaniclastic deposits-influences of initiation mechanisms and transport behavior on characteristics and distributions; *Geol. Soc. London, Spec. Publ.* **520**.

Manville V, Németh K and Kano K 2009 Source to sink: A review of three decades of progress in the understanding of volcaniclastic processes, deposits, and hazards; *Sediment. Geol.* **220** 136–161.

Mavoungou L N, Das K, Kawaguchi K, Hayasaka Y and Shibata T 2022 Back-arc basin closure at the East Asian margin during Permo-Triassic boundary: Evidence from geochemistry and U-Pb zircon data of sedimentary breccia from Maizuru Terrane, Southwest Japan; *Geosyst. Geoenviron.* **1(3)** 100080, https://doi.org/10.1016/j.geogeo.2022.100080.

McCaffrey W D, Kneller B C and Peakell J 2001 Particulate Gravity Currents; *Int. Assoc. Sediment.* **30** 302.

McLennan S M, Taylor S R, McCulloch M T and Maynard J B 1990 Geochemical and Nd– Sr isotopic composition of deep-sea turbidites: Crustal evolution and plate tectonic associations; *Geochim. Cosmochim. Acta* **54** 2015–2050.

McLennan S M and Hemming S 1992 Samarium/neodymium elemental and isotopic systematics in sedimentary rocks; *Geochim. Cosmochim. Acta* **56** 887–898.

McLennan S M, Hemming S, McDaniel D K and Hanson G N 1993 Geochemical approaches to sedimentation, provenance, and tectonics; *Geol. Soc. Am. Spec. Pap.* **284** 1–40.

McPhie Jocelyn M and Doyle R A 1993 Volcanic textures: A guide to the interpretation of textures in volcanic rocks.

Meinhold G, Kostopoulos D and Reischmann T 2007 Geochemical constraints on the provenance and depositional setting of sedimentary rocks from the islands of Chios, Inousses and Psara, Aegean Sea, Greece: Implications for the evolution of Palaeotethys; *J. Geol. Soc. London.* **164** 1145–1163.

Miall A D 1970 Devonian alluvial fans, Prince of Wales Island, Arctic Canada; *J. Sediment. Res.* **40**.

Middleton G V 1970 Experimental studies related to flysch sedimentation; Flysch Sedimentology North America; *Geol. Assoc. Can. Spec. Paper* **7** 253–272.

Miyabuchi Y 1999 Deposits associated with the 1990–1995 eruption of Unzen volcano, Japan; *J. Volcanol. Geotherm. Res.* **89** 139–158.

Morley C K 2002 A tectonic model for the Tertiary evolution of strike–slip faults and rift basins in SE Asia; *Tectonophysics* **347** 189–215.

Morley C K 1989 Extension, detachments, and sedimentation in continental rifts (with particular reference to East Africa); *Tectonics* **8** 1175–1192, https://doi.org/10.1029/TC008i006p01175.

Mueller W U and Corcoran P L 1998 Late-orogenic basins in the Archaean Superior Province, Canada: Characteristics and inferences; *Sediment. Geol.* **120** 177–203.

Mueller W, Chown E H and Thurston P C 2000 Processes in physical volcanology and volcaniclastic sedimentation: Modern and ancient; *Precamb. Res.* **101** 81–85.

Mukhopadhyay D, Bhattacharyya T, Chattopadhyay N, Lopez R and Tobisch O T 2023 Anasagar gneiss: A folded granitoid pluton in the Phanerozoic South Delhi Fold Belt, central Rajasthan; *J. Earth Syst. Sci.* **132**.

Naik A, Pant N C, Sharma J J, Bhandari A and Sorcar N 2022 Metamorphic evolution of the North Delhi Fold Belt, implications on Delhi orogeny and the Rodinia connection; *Geol. J.* **57(9)** 3496–3520.

Nemec W and Steel R J 1984 Alluvial and coastal conglomerates: Their significant features and some comments on gravelly mass-flow deposits; *Can. Soc. Pet. Geol. Mem.* **10** 1–31.

Pal T, Gupta T D, Chakraborty P P and Das Gupta S C 2005 Pyroclastic deposits of mio-pliocene age in the Arakan Yoma-Andaman-Java subduction complex, Andaman Islands, Bay of Bengal, India; *Geochem. J.* **39** 69–82.

Pearce J A 2008 Geochemical fingerprinting of oceanic basalts with applications to ophiolite classification and the search for Archean oceanic crust; *Lithos* **100** 14–48.

Peccerillo A and Taylor S R 1976 Geochemistry of Eocene calc-alkaline volcanic rocks from the Kastamonu area, northern Turkey; *Contrib. Mineral. Petrol.* **58** 63–81.

Raza M, Khan M and Azam M 2007 Plate-plume-accretion tectonics in Proterozoic terrain of northeastern Rajasthan, India: Evidence from mafic volcanic rocks of north Delhi fold belt; *Island Arc.* **16** 536–552.

Rogers J J W and Santosh M 2009 Tectonics and surface effects of the supercontinent Columbia; *Gondwana Res.* **15** 373–380, https://doi.org/10.1016/j.gr.2008.06.008.

Roverato M, Giordano D, Echeverri-Misas C M and Juliani C 2016 Paleoproterozoic felsic volcanism of the Tapajós Mineral Province, Southern Amazon Craton, Brazil; *J. Volcanol. Geotherm. Res.* **310** 98–106.

Roverato M, Juliani C, Dias-Fernandes C M and Capra L 2017 Paleoproterozoic andesitic volcanism in the southern Amazonian craton, the Sobreiro Formation: New insights from lithofacies analysis of the volcaniclastic sequences; *Precamb. Res.* **289** 18–30.

Sensharma S and Gaur R 2022 Origin of silicic breccio-conglomerate within the ∼2.5 Ga LIP rhyolites, Bastar craton (India) and its volcanological and stratigraphic implications; *J. Earth Syst. Sci.* **131(2)** 105.

Sharp T R and Robertson A H 2002 Petrography and provenance of volcaniclastic sands and sandstones recovered from the Woodlark rift basin and Trobriand forearc basin, Leg 180, Ocean Drilling Program.

Shields G A, Strachan R A, Porter S M, Halverson G P, Macdonald F A, Plumb K A and Zhu M 2022 A template for an improved rock-based subdivision of the pre-Cryogenian timescale; *J. Geol. Soc.* **179(1)**.

Shultz A W 1984 Subaerial debris-flow deposition in the upper Paleozoic Cutler Formation, western Colorado; *J. Sediment. Res.* **54** 759–772.

Singh S P 1982 Stratigraphy of Delhi Supergroup in Bayana sub-basin, northeastern Rajasthan; *Geol. Surv. India* **112** 46–62.

Singh S P 1985 Fluvial and tidal sedimentation in the Proterozoic Alwar Group, Bayana sub-basin, Bharatpur district, Rajasthan; *Rec. Geol. Surv. India* **116** 89–101.

Singh S P 1988 Influence of basement tectonics on the Delhi sedimentation in the Bayana graben, northeastern Rajasthan; *J. Geol. Soc. India* **32** 468–476.

Singh S P 1991 Paleogeography and clastic dispersal of the Proterozoic Delhi Supergroup in the Bayana sub-Basin. Northeastern India; *J. Indian Assoc. Sedimentol.* **10** 19–36.

Sohn Y K, Rhee C W and Kim B C 1999 Debris flow and hyperconcentrated flood-flow deposits in an alluvial fan, northwestern part of the Cretaceous Yongdong Basin, Central Korea; *J. Geol.* **107** 111–132.

Sohn C and Sohn Y K 2019 Distinguishing between primary and secondary volcaniclastic deposits; *Sci. Rep.* **9** 1–7.

Sparks R S J 1976 Grain size variations in ignimbrites and implications for the transport of pyroclastic flows; *Sedimentology* **23** 147–188.

Sparks R S J, Self S and Walker G P L 1973 Products of ignimbrite eruptions; *Geology* **1** 115–118.

Stern R J, Ren M, Kelley K A, Ohara Y, Martinez F and Bloomer S H 2014 Basaltic volcaniclastics from the Challenger Deep forearc segment, Mariana convergent margin: Implications for tectonics and magmatism of the southernmost Izu–Bonin–Mariana arc; *Island Arc.* **23(4)** 368–382.

Sulpizio R, Dellino P, Doronzo D M and Sarocchi D 2014 Pyroclastic density currents: State of the art and perspectives; *J. Volcanol. Geotherm. Res.* **283** 36–65.

Sun S S and McDonough W F 1989 Chemical and isotopic systematics of oceanic basalts: Implications for mantle composition and processes; *Geol. Soc. London Spec. Publ.* **42** 313–345.

Tarney J 1992 Geochemistry and significance of mafic dyke swarms in the proterozoic; *Dev. Precamb. Geol.* **10** 151–179, https://doi.org/10.1016/S0166-2635(08)70118-X.

Taylor S R and McLennan S M 1985 The continental crust: Its composition and evolution*; Geol. Magazine.*

Thompson R N, Morrison M A, Dickin A P and Hendry GL 1983 Continental flood basalts... arachnides rule OK?, In: UK Volcanic Studies Group Meeting 158–185.

Tsunogae T, Liu S J, Santosh M, Shimizu H and Li J H 2011 Ultrahigh-temperature metamorphism in Daqingshan, inner Mongolia suture zone, North China Craton; *Gondwana Res.* **20** 36–47.

Versfelt J and Rosendahl B R 1989 Relationships between pre-rift structure and rift architecture in Lakes Tanganyika and Malawi, East Africa; *Nature* **337** 354–357.

Walker G P L, Wright J V, Clough B J and Booth B 1981 Pyroclastic geology of the rhyolitic volcano of La Primavera, Mexico; *Geol. Rundschau* **70** 1100–1118.

White J D L and Houghton B F 2006 Primary volcaniclastic rocks; *Geology* **34** 677–680.

White R and McKenzie D 1989 Magmatism at rift zones: The generation of volcanic continental margins and flood basalts; *J. Geophys. Res. Solid Earth* **94** 7685–7729.

White W M 2000 Geochemistry; *Kirk-Othmer Encycl. Chem. Technol.*, pp. 1–36.

Winchester J A and Floyd P A 1977 Geochemical discrimination of different magma series and their differentiation products using immobile elements; *Chem. Geol.* **20** 325–343.

Wang H and Mo X 1995 An outline of the tectonic evolution of China; *Episodes J. Int. Geosci.* **18** 6–16.

Winter J D 2013 Principles of igneous and metamorphic petrology, Pearson education, 702p.

Wolff J A and Wright J V 1981 Rheomorphism of welded tuffs; *J. Volcanol. Geotherm. Res.* **10** 13–34.

Wright J V and Walker G P L 1981 Eruption, transport and deposition of ignimbrite: A case study from Mexico; *J. Volcanol. Geotherm. Res.* **9** 111–131.

Xiang Z, Yan Q, White J D L, Song B and Wang Z 2015 Geochemical constraints on the provenance and depositional setting of Neoproterozoic volcaniclastic rocks on the northern margin of the Yangtze Block, China: Implications for the tectonic evolution of the northern margin of the Yangtze Block; *Precamb. Res.* **264** 140–155.

Yokoyama T, Makishima A and Nakamura E 1999 Evaluation of the coprecipitation of incompatible trace elements with fluoride during silicate rock dissolution by acid digestion; *Chem. Geol.* **157(3–4)** 175–187, https://doi.org/10.1016/S0009-2541(98)00206-X.

Zhai M G and Santosh M 2011 The early Precambrian odyssey of the North China Craton: A synoptic overview; *Gondwana Res.* **20** 6–25.

Zhai M, Hu B, Zhao T, Peng P and Meng Q 2015 Late Paleoproterozoic-Neoproterozoic multi-rifting events in the North China Craton and their geological significance: A study advance and review; *Tectonophysics* **662** 153–166.

Zhang S H, Zhao Y and Santosh M 2012 Mid-mesoproterozoic bimodal magmatic rocks in the northern North China Craton: Implications for magmatism related to breakup of the Columbia supercontinent; *Precamb. Res.* **222** 339–367.

Zhao G, Cawood P A, Wilde S A and Sun M 2002 Review of global 2.1–1.8 Ga orogens: Implications for a pre-Rodinia supercontinent; *Earth-Sci. Rev.* **59** 125–162, https://doi.org/10.1016/S0012-8252(02)00073-9.

Zhao G, Sun M, Wilde S A and Li S 2003 Assembly, accretion and breakup of the Paleo-mesoproterozoic Columbia supercontinent: Records in the North China Craton; *Gondwana Res.* **6** 417–434, https://doi.org/10.1016/S1342-937X(05)70996-5.

Zhao G and Zhai M 2013 Lithotectonic elements of Precambrian basement in the North China Craton: Review and tectonic implications. *Gondwana Res.* **23** 1207–1240.

Corresponding editor: N V Chalapathi Rao